

A NEW DIAGNOSTIC OF ACTIVE GALACTIC NUCLEI: REVEALING HIGHLY-ABSORBED SYSTEMS AT REDSHIFT > 0.3

STÉPHANIE JUNEAU

Steward Observatory, University of Arizona, Tucson, AZ 85721; sjuneau@as.arizona.edu

MARK DICKINSON

National Optical Astronomy Observatory, 950 North Cherry Avenue, Tucson, AZ 85719; med@noao.edu

DAVID M. ALEXANDER

Department of Physics, Durham University, Durham DH1 3LE, UK; d.m.alexander@durham.ac.uk

AND

SAMIR SALIM

Department of Astronomy, Indiana University, Bloomington, IN 47404; salims@indiana.edu

To appear in the ApJ

ABSTRACT

We introduce the Mass-Excitation (MEx) diagnostic to identify active galactic nuclei (AGNs) in galaxies at intermediate redshift. In the absence of near-infrared spectroscopy, necessary to use traditional nebular line diagrams at $z > 0.4$, we demonstrate that combining $[\text{O III}] \lambda 5007/\text{H}\beta$ and stellar mass successfully distinguishes between star formation and AGN emission. The MEx classification scheme relies on a novel probabilistic approach splitting galaxies into sub-categories with more confidence than alternative high- z diagnostic diagrams. It recognizes that galaxies near empirical boundaries on traditional diagrams have an uncertain classification and thus a non-zero probability of belonging to more than one category. An outcome of this work is a system of statistical weights that can be used to compute global properties of galaxy samples. We apply the MEx diagram to 2,812 galaxies at $0.3 < z < 1$ in the Great Observatories Origins Deep Survey North and Extended Groth Strip fields, and compare it to an independent X-ray classification scheme. We identify Compton-thick AGN candidates with large X-ray absorption, which we infer from the luminosity ratio between hard X-ray emission and $[\text{O III}] \lambda 5007$, a nearly isotropic tracer of AGN. X-ray stacking of sources that were not detected individually supports the validity of the MEx diagram and yields a very flat spectral slope for the Compton-thick candidates ($\Gamma \approx 0.4$, unambiguously indicating absorbed AGN). We present evidence that composite galaxies, which are difficult to identify with alternative high-redshift diagrams, host the majority of the highly-absorbed AGN. Our findings suggest that the interstellar medium of the host galaxy provides significant absorption in addition to the torus invoked in AGN unified models.

Subject headings: galaxies: active — galaxies: evolution — galaxies: fundamental parameters and ISM — galaxies: high-redshift — X-rays: galaxies

1. INTRODUCTION

Most if not all galaxies contain a supermassive black hole (SMBH) in their center (Richstone et al. 1998), which follow fundamental relations to their host galaxies (Magorrian et al. 1998; Ferrarese & Merritt 2000). Furthermore, the accretion history of supermassive black holes follow a similar, scaled-down, trend as the cosmic star formation history (Barger et al. 2001). Taken together, these observations strongly suggest that black hole accretion and star formation may be linked phenomena. In particular, active galactic nuclei (AGNs) have been invoked in galaxy evolution models as a means to control the rate of star formation in galaxies via feedback (e.g., Croton et al. 2006; Narayanan et al. 2008). While some observational evidence is provided by, e.g., high-velocity outflows in post-starburst galaxies (Tremonti et al. 2007), the full picture on the interplay between AGN and their host galaxies remains unclear.

A complete understanding of galaxy evolution re-

quires the study of both galaxy stellar content and nuclear activity. However, differentiating the powering source – star formation versus AGN – poses an appreciable challenge. While there are several independent tracers of AGN, all suffer from limitations. Because the caveats of one tracer can be overcome by the strength of another, it has become clear that multi-wavelength methods are required to assess the ubiquity of AGNs. For example, X-ray emission has been used extensively to uncover and study large populations of AGNs (Bade et al. 1995; Boyle et al. 1993; Brandt et al. 2001). However, even the most sensitive X-ray surveys still miss heavily absorbed systems. These absorbed AGNs were inferred by the unresolved portion of the cosmic X-ray background, which shows a flat X-ray spectral slope highly suggestive of X-ray absorption (Comastri et al. 1995; Mushotzky et al. 2000; Alexander et al. 2003; Bauer et al. 2004; Treister & Urry 2005).

This scenario is supported by the existence of Compton-thick systems in the nearby universe that would not be detected in the most sensitive X-ray surveys if they were at higher redshift, e.g., NGC 1068. This galaxy was also shown to have X-ray absorbers on a scale of the order of ~ 1 pc (Guainazzi et al. 2000).

Even if X-ray photons are absorbed or scattered by material on a compact scale such as the torus component described in the *unified model* (Antonucci 1993), emission originating from larger scales may reach the observer regardless of the line of sight. Such isotropic tracers include emission lines from the narrow line regions, which are exterior to the torus. Commonly used lines include [O III] $\lambda 5007$ in the optical (Baldwin et al. 1981; Busko & Steiner 1988) and [O IV] $\lambda 25.9\mu\text{m}$ or [Ne V] $\lambda 14\mu\text{m}$ in the infrared regime (Sturm et al. 2002; Armus et al. 2004, 2007; Diamond-Stanic et al. 2009; Rigby et al. 2009; LaMassa et al. 2010). Another such tracer is mid-infrared continuum emission originating from hot dust heated by the AGN (e.g., Lacy et al. 2004; Stern et al. 2005; Donley et al. 2007). This method works especially well for intrinsically luminous AGN that are deeply enshrouded, but does not select the less-luminous systems which may still be absorbed. Mid-infrared aromatic features can also be used to diagnose the powering source in galaxies (Genzel et al. 1998; Lutz et al. 1998; Pope et al. 2008).

On the one hand, some of the distinctions between the classes of AGNs and the selection methods listed above are thought to arise from their orientation with respect to the observer’s line of sight. On the other hand, some AGN classes seem to comprise physically distinct phases of activity (i.e., low versus high accretion rate, beginning or end of an active phase). The latter are more interesting from the point-of-view of galaxy evolution as they may provide a handle on the importance of AGN phases, their duty cycle, and the interplay between AGNs and their host galaxies.

One example of physically-distinct AGN phases are Seyferts and low-ionization nuclear emission line regions (LINERs). These two categories emerged from optical spectroscopy studies where emission lines with different excitation properties were used as probes of the radiation exciting the interstellar gas (Seyfert 1943; Heckman 1980). In addition to exhibiting specific spectral signatures, Seyfert and LINER nuclei were found to reside in distinct host galaxies compared to star-forming galaxies and also relative to one another. Kauffmann et al. (2003) showed that galaxies hosting an AGN tend to have a larger stellar mass compared to star-forming galaxies that lack optical AGN signatures. Galaxies with a Seyfert nucleus (or Seyferts for short) often have a young or intermediate-age component in their stellar population whereas galaxies with LINER emission have, on average, an older stellar population as well as a larger stellar mass than Seyferts (e.g. Kewley et al. 2006). Putting this evidence together with the observations that AGNs seem to follow a decreasing sequence in accretion rate from Seyferts to LINERs to composite galaxies (Ho 2008) suggests an evolutionary picture where LINERs may be older, dying, AGNs relative to Seyferts.

Whether this emerging picture is supported by higher-redshift observations is unclear. At larger distances, it is generally more difficult to get a complete cen-

sus of galaxies with AGNs, let alone to classify them in different AGN categories/phases. Gathering complete samples of galaxies for which we know the powering source, and whether the central black hole is actively accreting, is especially challenging at $z > 0.4$. Beyond that redshift, optical emission lines needed for AGN classification such as H α and [N II] $\lambda 6584$ are shifted into the near-infrared, preventing the application of well-calibrated, traditional diagnostics (Baldwin et al. 1981; Veilleux & Osterbrock 1987; Kewley et al. 2001; Kauffmann et al. 2003; Kewley et al. 2006; Stasińska et al. 2006).

In this paper, we present the Mass-Excitation (MEx) diagnostic diagram, based in part on optical nebular lines that can readily be observed out to $z \sim 1$. Following a similar method as Weiner et al. (2007), who replaced the [N II] $\lambda 6584$ /H α line flux ratio used in the BPT diagram (Baldwin et al. 1981) with absolute *H*-band magnitude, we adopt stellar mass as a substitute for [N II] $\lambda 6584$ /H α . We will show that a better census of AGN can be obtained by finding both intrinsically weak AGNs as well as absorbed systems that are undetected in X-ray observations. Our classification scheme relies on a novel probabilistic approach and allows us to split the galaxies into the following categories: purely star-forming galaxies, Seyfert 2s, LINERs or composite systems (i.e., with both star-formation and AGN). Galaxies near the empirical boundaries on traditional diagnostic diagrams have a less certain classification and are thus assigned a non-zero probability of belonging to more than one category. As a result, the MEx diagnostic also outputs statistical weights that can be utilized to compute global properties (e.g., stellar mass, metallicity, etc.) in statistical samples of galaxies belonging to any of the categories listed above.

Using a sample of low-redshift galaxies described in §2, we calibrate our diagnostic in §3.1. We briefly analyze the occurrence of low-ionization nuclear emission-line regions (LINERs) in §3.2 before introducing a novel approach to galaxy spectral classification based on the probability of each spectral class (e.g., star-forming or AGN, §3.3). We describe our $0.3 < z < 1$ galaxy sample in §4, and the application of our new Mass-Excitation (MEx) diagram in §5. We find an excellent agreement between the MEx diagram and the X-ray classification (§5.1). We examine the different optical and X-ray classes more closely with an X-ray stacking analysis (§5.2). Combining hard X-ray emission and optical emission lines allow us to probe the X-ray absorption leading to the discovery of Compton-thick AGNs among our intermediate-redshift sample §6. We compare the MEx diagram with alternative AGN diagnostic diagrams in §7.1 and we describe how the new method contributes to achieving a more complete census of AGNs (§7.2). We discuss the fraction of AGNs that suffer from X-ray absorption (§7.4) and possible evolution effects on emission-line AGN diagnostics in §7.5 before summarizing our main conclusions in §8. We assume a flat cosmology with $\Omega_m = 0.3$, $\Omega_\Lambda = 0.7$, and $h = 0.7$ throughout.

2. LOW-REDSHIFT GALAXY SAMPLE

Our low-redshift calibration sample comes from the Sloan Digital Sky Survey (SDSS; York et al. 2000). The limiting magnitude of the spectroscopic sample is $r < 17.7$. Our analysis is based on data products from Data

Release 4 (Adelman-McCarthy et al. 2006), namely the value-added galaxy catalogs¹ from the Max-Planck Institute for Astronomy (Garching) and John Hopkins University. In these catalogs, the stellar masses are calculated as described in Kauffmann et al. (2003) assuming a Kroupa (2001) initial mass function (IMF), while emission line measurements follow the procedures from Tremonti et al. (2004).

In order to avoid strong aperture bias due to SDSS fiber size, we constrain the redshift range to $0.05 < z < 0.2$. This lower limit corresponds to a minimum covering fraction $\sim 30\%$. Kewley & Ellison (2008) found that using a covering fraction down to 20% ($z \sim 0.04$) is not sufficient to obtain global emission line properties for massive galaxies (with $M_\star > 10^{10} M_\odot$). That is why we adopt a stricter requirement here.

Imposing a signal-to-noise ratio cut $S/N > 3$ on all emission lines to be used in the diagnostic diagrams ($[\text{O II}] \lambda 3727$, $\text{H}\beta$, $[\text{O III}] \lambda 5007$, $\text{H}\alpha$, $[\text{N II}] \lambda 6584$ and $[\text{S II}] \lambda \lambda 6717, 6731$; §3.1), we obtain a sample of 110,205 emission-line galaxies.

3. EMISSION-LINE DIAGNOSTIC DIAGRAMS

Here we aim to create a modified version of the BPT² diagram, involving $[\text{N II}] \lambda 6584/\text{H}\alpha$ and $[\text{O III}] \lambda 5007/\text{H}\beta$, by replacing the ratio of the redder emission lines ($[\text{N II}] \lambda 6584/\text{H}\alpha$) because they shift into the near-infrared at $z > 0.4$. To that purpose, we introduce the Mass-Excitation (MEx) diagram below, which we will subsequently apply to intermediate redshift galaxies ($0.3 < z < 1$) in §5.

3.1. Calibration Using $z \sim 0.1$ SDSS Galaxies

In this section, we introduce and calibrate the Mass-Excitation diagram and compare it to one of the original BPT diagrams. The emission line ratios used in the best-known version of this diagram ($[\text{N II}] \lambda 6584/\text{H}\alpha$ and $[\text{O III}] \lambda 5007/\text{H}\beta$) probe a combination of the ionization parameter and the gas-phase metal abundance within galaxies. As shown in Figure 1(a), SDSS galaxies form a well-defined excitation sequence on the lower-left of the BPT diagram (below the semi-empirical dividing curve from Kauffmann et al. 2003, solid line), while the galaxies containing AGN form a plume extending to the top right part of the diagram. The higher ionization parameter and/or harder ionizing radiation that occur only in the presence of AGN cause the line ratios to lie above and to the right of the maximum starburst curve (dashed line) developed by Kewley et al. (2001). Galaxies that are located between both curves are believed to host a mixture of star-formation and AGN and are sometimes called composites. We adopt this nomenclature in the remainder of this work.

While the BPT diagram shown in Figure 1(a) is used extensively to identify the source of ionization in galaxies, the $[\text{N II}]$ and $\text{H}\alpha$ emission lines become unavailable in optical spectra at $z > 0.4$. What would be a good substitute for $[\text{N II}]/\text{H}\alpha$? The $[\text{N II}]/\text{H}\alpha$ line ratio provides an indication of the gas-phase metallicity in star-forming galaxies (Kewley & Ellison 2008). The empiri-

cal mass-metallicity relation (e.g., Tremonti et al. 2004; Savaglio et al. 2005) suggests a physical connection between that line ratio and the stellar mass, as displayed in Figure 1(b). While the $M_\star - Z$ relation applies to star-forming galaxies without AGNs, there is another effect that makes stellar mass a good choice. The $[\text{N II}]/\text{H}\alpha$ ratio saturates at high values for normal star-forming galaxies and only more extreme conditions such as those encountered in the presence of an AGN can yield larger values (Kewley et al. 2006; Stasińska et al. 2006). Because AGNs tend to be found in hosts with high stellar mass (Kauffmann et al. 2003), these systems have both larger $[\text{N II}]/\text{H}\alpha$ and M_\star values. This feature puts them in a location of the parameter space of the modified diagram that is analogous to their original location on the BPT diagram with respect to purely star-forming galaxies (i.e., higher and to the right). Consequently, the new AGN diagnostic is obtained by substituting stellar mass for the redder emission line ratio.

Indeed, we find that the BPT-SF and BPT-AGN classes are well separated on the new Mass-Excitation (MEx) diagram (Figure 1(c)). We define two empirical dividing lines that maximize the separation between galaxy classes, especially between the BPT-AGN class (above and to the right of the lines) and the purely star-forming BPT-SF class (below and to the left of the dividing lines). We note that the location of the BPT-composite galaxies on the MEx diagram overlap with galaxies belonging to the other classes as shown in Figure 1(d). Their locus peaks in the region between the two empirical curves, which we dub the MEx-intermediate region. We note that 48% of the galaxies in this region are BPT-composites.

The number of galaxies of each BPT-class are reported in Table 1 for the three regions of the MEx diagram, and the main empirical division (top curve) is defined as follows:

$$y = \begin{cases} 0.37/(x - 10.5) + 1. & \text{if } x \leq 9.9 \\ a_0 + a_1x + a_2x^2 + a_3x^3 & \text{otherwise,} \end{cases} \quad (1)$$

where $y \equiv \log([\text{O III}] \lambda 5007/\text{H}\beta)$ and $x \equiv \log(M_\star)$. The coefficients are the following: $\{a_0, a_1, a_2, a_3\} = \{594.753, -167.074, 15.6748, -0.491215\}$. Similarly, the lower curve defined as:

$$y = 800.492 - 217.328x + 19.6431x^2 - 0.591349x^3, \quad (2)$$

and is used over the range $9.9 < x < 11.2$.

Using the BPT classes as our reference, we compute the completeness and contamination fractions of the MEx selection for both the AGN and SF classes, separated using Eq. 1. The fractions are displayed in Figure 2. For the MEx-AGN class, we find that the completeness is very high in terms of BPT-AGNs (i.e., above the Kewley et al. (2001) line), reaching close to 100% at high stellar mass (see the red diamonds in the top panel of Figure 2). The fraction of BPT-composite galaxies that are selected in the MEx-AGN side rises more slowly with stellar mass: from $\sim 20\%$ at $M_\star < 10^{10} M_\odot$ to 95% at $M_\star > 10^{11.5} M_\odot$ (black triangles). In the top panel, the contamination fraction is defined as the fraction of BPT-SF galaxies (below the Kauffmann et al. (2003) line) in the MEx-AGN side. The contamination fraction peaks at 10-20% for galaxies with $M_\star \sim 10^{10} M_\odot$, but it mostly stays well

¹ <http://www.mpa-garching.mpg.de/SDSS/DR4/>

² Named after the last names of the three authors who introduced it: Baldwin-Phillips-Terlevich (Baldwin et al. 1981)

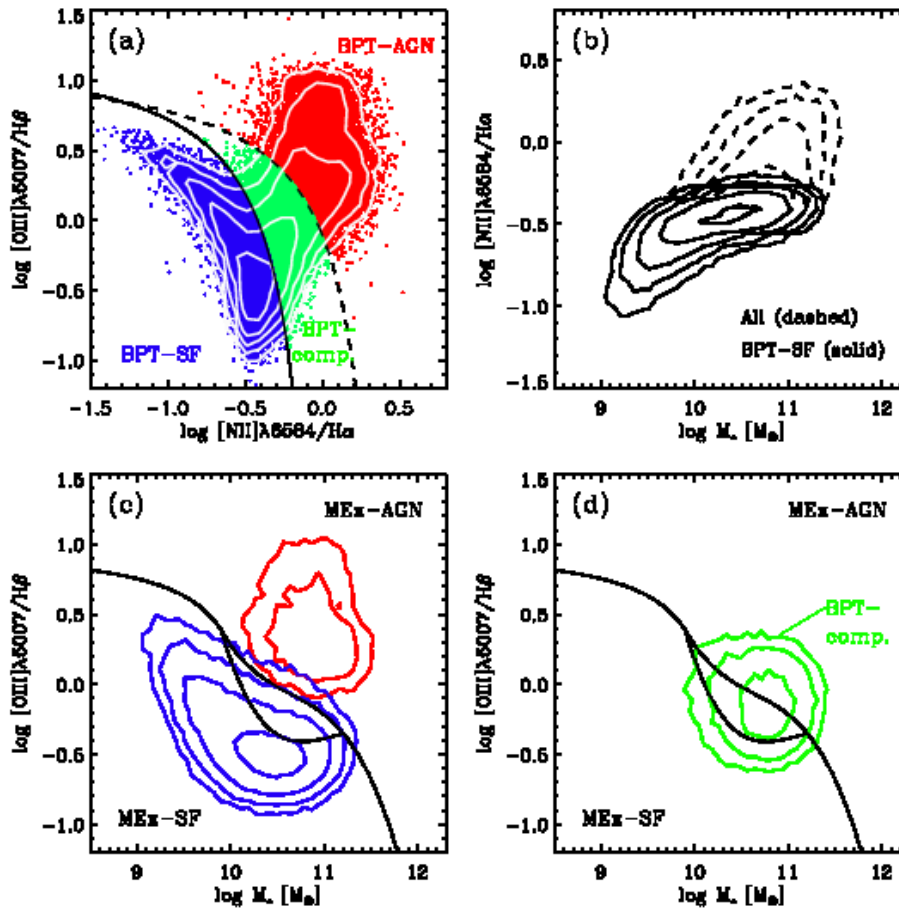


FIG. 1.— Emission line diagnostic diagrams: (a) BPT diagram: purely star-forming galaxies (SF, shown in blue) form a sequence below the solid line adapted from Kauffmann et al. (2003) whereas galaxies hosting an AGN (red) tend to occupy the area above and to the right of the dashed curve (Kewley et al. 2001). Galaxies located between the two curves are composites, i.e., having mixed SF and AGN contributions (BPT-comp., green). (b) Stellar mass as a function of the line ratio $[\text{N II}] \lambda 6584 / \text{H}\alpha$. For star-forming galaxies the trend is analogous to the $M_* - Z$ relation (solid contours). For the total sample including composites and AGNs, there is a stronger increase in $[\text{N II}] / \text{H}\alpha$ compared to stellar mass but AGNs reside in galaxies with both a high value of $[\text{N II}] / \text{H}\alpha$ and a high stellar mass. These two features indicate that stellar mass is a viable substitute when $[\text{N II}] \lambda 6584$ or $\text{H}\alpha$ are not available. The modified diagnostic diagram is shown in (c) for the galaxies classified as SF or AGN on the BPT diagram (blue and red contours, respectively) and in (d) for those classified as composites (green contours). The MEx-intermediate region, located between the two empirical curves on the MEx diagram, contains a mix of composites (BPT-comp.) and star-forming (BPT-SF) galaxies. In all panels, the contours indicate the density of points (in bins of $0.075 \text{ dex} \times 0.075 \text{ dex}$) and are logarithmic (0.5 dex apart, with the outermost contour set to 10 galaxies per bin). (A color version of this figure is available in the online journal.)

below 10%, with an overall fraction around 6% (blue asterisks). Global completeness and contamination values, calculated for the entire SDSS sample (all stellar masses), are shown with the larger plotting symbols on the right hand side of the figure.

Similarly, the completeness for the MEx-SF selection is defined as the fraction of the BPT-SF galaxies that are correctly identified. The completeness is close to 100% (blue asterisks in Figure 2[b]) over a wide range of stellar masses with a drop off at $M_* > 10^{11} M_\odot$. We note that at such high masses, there are very few purely star-forming galaxies (~ 200 and < 10 in the last two bins) whereas there are of the order of 10^4 galaxies per bin at lower mass (Figure 2[c]). The contamination with the BPT-AGN class is extremely low (red diamonds), on the order of 0.3%. However, the contamination fraction for BPT-composite goes up to $\sim 30\%$ at $M_* > 10^{11} M_\odot$. These galaxies lie mostly in the intermediate region of the MEx diagram. Whether they should be included with the star-forming sample or rejected will depend on

the specific science goal.

We report the numbers for the MEx-intermediate class (i.e., between the lines defined by Eq. 1 and 2) separately in Table 1. Even though the AGN contamination of the MEx-SF class appears to be more substantial at high stellar mass, the effect is exaggerated by the small number of purely star-forming galaxies with $M_* > 10^{11} M_\odot$. In fact, the AGN completeness peaks at the same mass range where the MEx-SF class appears the most contaminated, indicating that overall, the majority of the most massive galaxies harbor an AGN. Conversely, very few AGNs reside in low- M_* hosts.

The scarcity of BPT-AGNs in host galaxies with $M_* < 10^{10} M_\odot$ was previously noted by Kauffmann et al. (2003). These authors found that adding the emission from low-luminosity AGNs (with $10^5 < L_{[\text{O III}] \lambda 5007} < 10^6 L_\odot$) to low- M_* star-forming galaxies would significantly alter their line ratios and move the corresponding points into the composite or AGN regions of the BPT diagram (in 93% of the cases with low-luminosity

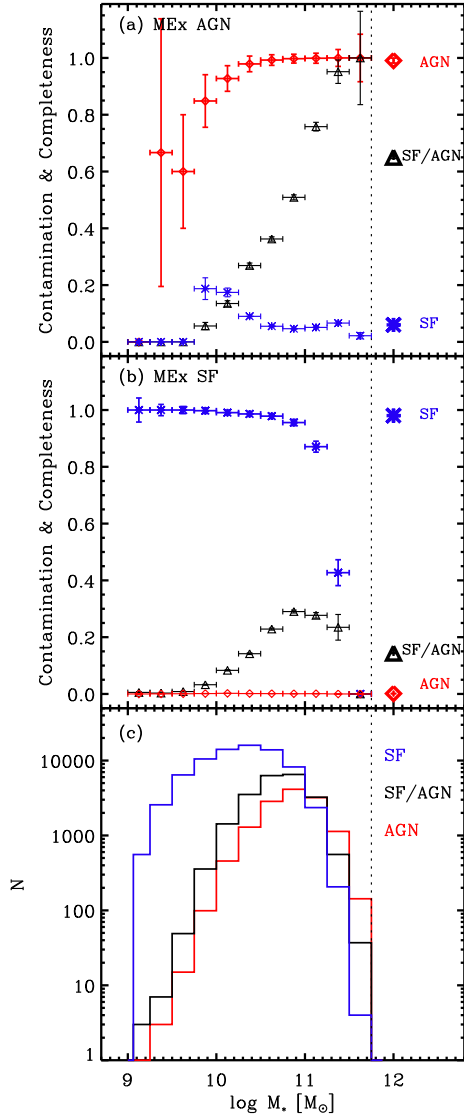


FIG. 2.— Completeness and contamination rates in bins of stellar mass (0.25 dex bins). *Top*: For the MEx-AGN selection, the AGN completeness is defined as the percentage of BPT-AGNs (above the Kewley line in the BPT diagram) that are above the MEx diagram dividing line (red diamonds). The definition is similar for the BPT-composite galaxies (black triangles). The contamination rate corresponds to the percentage of galaxies in the AGN side of the MEx diagram that would be purely star-forming galaxies according to the BPT diagram (blue asterisks). The overall values for the entire stellar mass range are shown on the right hand side of the figure. *Middle*: For the MEx-SF selection, the completeness is defined as the percentage of BPT-SF galaxies (below the Kauffmann line) that are correctly identified in the star-forming side. The contamination rates are computed separately for the BPT-AGNs (red diamonds) and BPT composites (black triangles) and correspond to percentage of the number of galaxies in the star-forming side of the MEx diagram. Error bars are Poissonian. *Bottom*: Distribution of stellar masses for galaxies that are classified as star-forming (blue), AGN (red), or composite (black). (A color version of this figure is available in the online journal.)

AGNs, and $>99\%$ for high-luminosity AGNs, i.e., with $L_{[\text{O III}]\lambda 5007} > 10^7 L_\odot$.

So far, we have used the BPT spectral types (SF, AGN, composites) as references to quantify the completeness and contamination rates of the MEx selection. Now, we turn the situation around and we show a graphical comparison of the MEx diagram selection (eq. 1) mapped back onto the usual BPT diagram. Figure 3(a) shows the classification on the MEx diagram with MEx-AGN and MEx-SF galaxies colored in orange and purple, respectively. The contours show the density of points on a logarithmic scale. As can be seen in panel (b), our new AGN selection (orange contours) picks all the AGNs from the BPT diagram (above the dashed line in panel (b)) as well as a fair number of BPT-composites (mostly at higher $[\text{O III}]\lambda 5007/\text{H}\beta$ ratio), whereas our new MEx-SF selection (purple contours) captures the BPT star-forming sequence extremely well, with an extension into the BPT-composite region between the two dividing lines, especially in the region close to the Kauffmann et al. (2003) solid line. Galaxies in the MEx-intermediate region (light purple dots) are distributed over the BPT-comp. and BPT-SF regions.

3.2. A closer look at LINERs

The nature of LINERs remains controversial. Historically, they have been identified by the unusual strength of their narrow optical emission lines with low-ionization potential (Heckman 1980). While most studies consider that LINERs are accretion-powered (Ho 1999; Kewley et al. 2006), there are also claims that, in some cases, the powering source could be entirely stellar (e.g., from post-AGB stars and/or white dwarfs, Binette et al. 1994; Stasińska et al. 2008) or a combination of processes including shocks (Heckman 1980). Eracleous et al. (2010) argue that AGN activity does not provide enough energy to produce the LINER emission in half of their X-ray-selected sample of 35 LINERs. Such a deficit had been suggested previously (e.g., Ho et al. 1993), and could be compensated by either obscuration of UV photons from the AGN, or by contributions from alternative sources such as post-AGB stars.

Chandra X-ray observations have been used to look for X-ray cores within LINERs. The detection fraction is typically high, ranging from 50% to 70% (see the review by Ho 2008, and references therein). Employing *Spitzer* spectroscopy, Dudik et al. (2009) searched for high-ionization lines associated with AGN activity ($[\text{Ne V}]\lambda 14$ and $24\mu\text{m}$). They find that 39% of their sample of 67 LINERs have such detections and that many of these cases lack AGN signatures at optical and X-ray wavelengths. They also show that the optical identification (from, e.g., broad $\text{H}\alpha$ lines) is more subject to fail at higher infrared luminosities, suggesting that some AGNs may be missed due to dust obscuration. Their AGN fraction in LINERs goes up to 74% after combining diagnostics in all three wavelength ranges (X-ray, optical, mid-IR).

The BPT diagram that includes $[\text{O III}]\lambda 5007/\text{H}\beta$ against $[\text{S II}]\lambda\lambda 6717, 6731/\text{H}\alpha$, hereafter the $[\text{S II}]$ diagram, can be used to tell apart the LINERs from the Seyfert 2 (Sy2) galaxies (e.g., Kewley et al. 2006). We apply this diagram to our SDSS sample in Figure 4. Panel (a) shows the $[\text{S II}]$ diagram with dividing lines be-

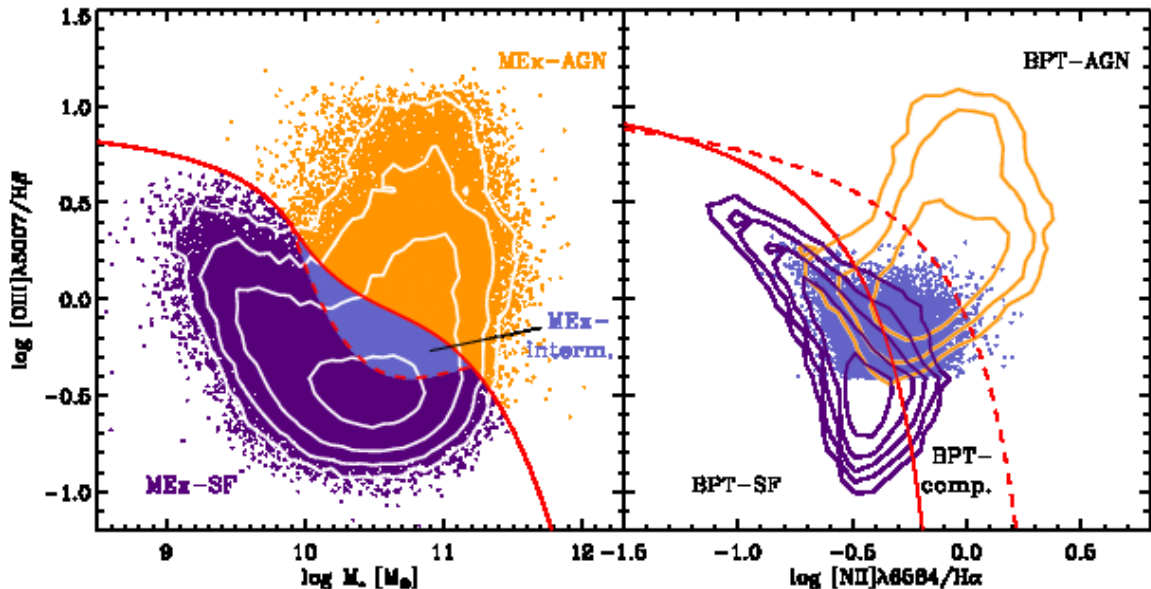


FIG. 3.— (left) Distribution of SDSS galaxies on the MEx diagram with our empirical divisions. Galaxies above the lines are classified as MEx-AGN (orange) whereas the galaxies below the lines are classified as star-forming (MEx-SF, in violet) and galaxies between the lines are MEx-intermediate (MEx-interm., in light purple). Using the same color-coding, we show these galaxies on the standard BPT diagram (right). Here, galaxies that are in the MEx-intermediate region are shown with dots while the MEx-SF and MEx-AGN subsamples are overplotted with contours (violet and orange, respectively). The contours indicate the density of points (in bins of $0.075 \text{ dex} \times 0.075 \text{ dex}$) and are logarithmic (0.5 dex apart, with the outermost contour set to 10 galaxies per bin). (A color version of this figure is available in the online journal.)

tween star-forming, Seyfert, and LINER populations as labeled. Seyfert 2 (in red) and LINER (in orange) galaxies as defined in the [S II] diagram overlap slightly on the [N II] (panel b) and MEx (panels c,d) diagrams. BPT-composites (between the lines on the BPT [N II] diagram) fall closer to the LINER than to the Sy2 distribution.

Composite galaxies stand out more in their [N II]/H α than in their [S II]/H α ratio. Consequently, the star-forming selection (blue contours) extends into the composite and AGN regions of the BPT and MEx diagrams [Figure 4(b) and (c)]. As mentioned previously, the [S II]/H α ratio has the advantage of splitting the LINERs from the Seyfert AGNs [dashed line from Kewley et al. (2006)]. This allows us to see that the MEx diagram selects both of these types of AGNs, and that the SDSS sample used here contains more LINERs than Seyfert 2's.

In the remainder of our analysis, we will use a scheme that combines the most trusted features of each diagram (i.e., the [N II] and the [S II] diagrams), which we introduce in the next section.

3.3. A Probabilistic Approach to Galaxy Classification

As was shown previously, some galaxy spectral classes overlap on the MEx diagram [Fig. 1(b,c); 3 and 4(c,d)]. Namely the MEx-intermediate region contains BPT-SF and BPT-composites, and there is also overlap between the BPT-LINERs and other AGN subclasses. To better assess the classification in such cases we present a scheme based on the probability of each spectral class given a galaxy's position on the MEx diagram. This approach is useful to discriminate between star-forming galaxies, composite galaxies, LINERs and Seyfert 2's.

In order to quantify the probabilities, we use a low-redshift³ SDSS sample as a calibration set. All of the

BPT diagnostic emission lines are available for these galaxies and we can place them on the MEx diagram with prior knowledge of their source of ionization. The source of ionization is assigned according to a hybrid classification based on both the [N II] and [S II] BPT diagrams with the following rules:

1. Star-Forming (SF): galaxies below the Kauffmann et al. (2003) line on the [N II] diagram irrespectively of their class on the [S II] diagram.
2. LINER: galaxies that are classified as AGN in the [N II] diagram (above the line from Kewley et al. 2001) or in the [S II] diagram and that are below and to the right of the Seyfert/LINER dividing line on the [S II] diagram (Eq. 13 of Kewley et al. (2006)).
3. Seyfert 2 (Sy2): galaxies that are classified as AGN in the [N II] diagram (above the line from Kewley et al. 2001) or in the [S II] diagram and that are above and to the left of the Seyfert/LINER dividing line on the [S II] diagram (Eq. 13 of Kewley et al. (2006)).
4. Composite (comp): composite galaxies from the [N II] diagram (between the (Kauffmann et al. 2003) and (Kewley et al. 2001) curves) that were not included in the LINER and Sy2 classes described above.

The resulting spectroscopically-classified sample is the *SDSS prior sample*, which we assume is representative of

³ $0.05 < z < 0.1$; The upper bound of the redshift range is chosen to remain complete in all categories including LINERs, whose detection rate decreases beyond $z \sim 0.1$ (Kewley et al. 2006).

³ $0.05 < z < 0.1$; The upper bound of the redshift range is cho-

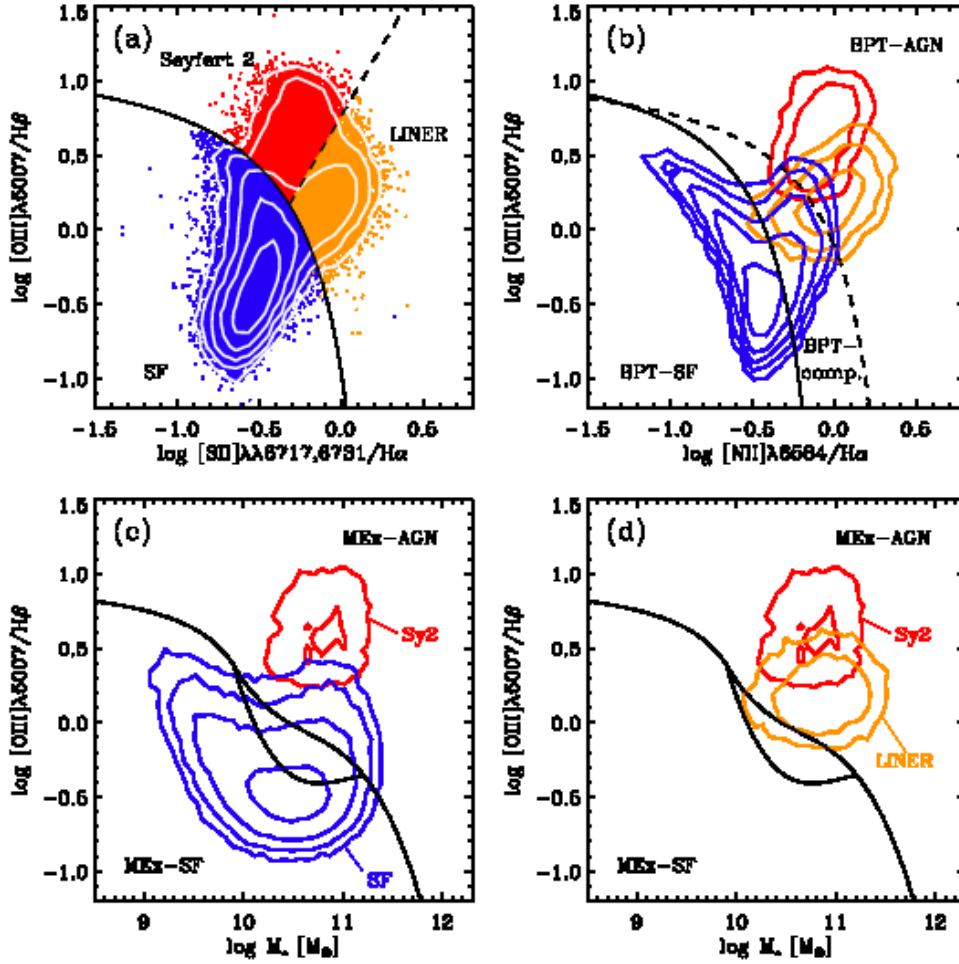


FIG. 4.— (a) The [S II] diagram. SDSS galaxies are color-coded according to their classification as SF (blue), Seyfert 2 (red) or LINER (orange). The dividing lines are taken from Kewley et al. (2006). All three classes are shown on the BPT diagram (b) with the same color scheme. The [S II] diagram is not very sensitive to composite galaxies (BPT-comp.) as most of them are classified as SF (blue contours). Similarly, the three [S II] diagram classes are shown on the MEx diagram (panel c) for the SF and Seyfert 2 galaxies, and panel (d) for the LINERs relative to the Seyfert 2’s). The upper empirical line on the MEx diagram selects all Sy2’s and LINERs on the AGN side (above the lines), with some overlap between the two classes. In all panels, contours indicate the density of points (in bins of $0.075 \text{ dex} \times 0.075 \text{ dex}$) and are logarithmic (0.5 dex apart, with the outermost contour set to 10 galaxies per bin). (A color version of this figure is available in the online journal.)

galaxies out to $z = 1$ (see §7.5 for a discussion of possible evolutionary effects).

Relative to the previous diagrams, the combined classification method yields a slightly greater number of AGNs than each of the [N II] and [S II] diagram taken separately (because we use the union of the two AGN subsamples). Correspondingly, the composite class is slightly less numerous because some composite galaxies from the [N II] diagram are selected as AGN based on the [S II] diagram (mostly in the LINER region). Another distinction is that the LINERs from the [S II] diagram that extend into the star-forming side of the [N II] diagram are now in the star-forming category. The latter category is identical to the original [N II] star-forming selection.

We now have a spectral classification scheme that exploits the strengths of both the [N II] and [S II] diagrams, and contains four mutually exclusive categories: star-forming (SF), composite (comp), LINER and Seyfert 2. We employ the distribution of the SDSS galaxies on the MEx diagram with *a priori* knowledge of their BPT classification to compute the fraction of galaxies of each cat-

egory across the MEx plane.

For galaxies at higher redshift for which only [O III] $\lambda 5007/H\beta$ and stellar mass (M_*) are available, we use the rectangular region on the MEx diagram defined by the one-sigma uncertainties on these two measurements. We compute the number of *SDSS prior* galaxies in each category (star-forming, composite, LINER, and Seyfert 2) and we normalize by the total number of *SDSS prior* galaxies within the rectangular box. The fractions are converted to percentages. Given that the four classes described above are mutually exclusive, the sum $P(SF) + P(comp) + P(LINER) + P(Sy2) = 100\%$. For example, if a region surrounding given values of [O III] $\lambda 5007/H\beta$ and M_* (defined by the one-sigma error bars) contains 20,000 SF galaxies; 10,000 composites; 10,000 LINERs and no Seyfert 2s in the SDSS prior sample, the assigned probabilities would be $P(SF) = 50\%$, $P(comp) = 25\%$, $P(LINER) = 25\%$, and $P(Sy2) = 0\%$. Thus, this probabilistic AGN classification scheme has a built-in uncertainty. This is a useful feature compared to alternative diagrams where there is often no knowledge

of the reliability of a certain classification. With this new approach, we know whether a given galaxy is near a dividing line or whether it is located far into the AGN or star-forming locus. In this paper, we assume that composites, LINERs, and Seyfert 2's all host an active nucleus and often use: $P(AGN) = 1 - P(SF)$ (equivalent to $P(AGN) = P(comp) + P(LINER) + P(Sy2)$).

The empirical division on the MEx diagram introduced earlier (§ 3.1) traces well the observed transition between SDSS galaxies that host AGN activity of any category (composite, LINER, or Seyfert 2) and galaxies that are most likely star-forming [Figure 5(a,b)]. Figure 5 shows the probabilities $P(SF)$ and $P(AGN)$ as a function of position on the MEx diagram. The lower dividing curve delineates the separation between a *cleaner* star-forming galaxy sample (below) and the MEx region where $P(AGN) > 30\%$ (above). The region between the two curves contains a mixed BPT-SF/BPT-composite population. We adopt the term MEx-intermediate to describe this region of the MEx diagram and the galaxies that are located within it.

An alternative diagnostic diagram, developed in parallel to the MEx diagram, involves the same emission-line ratio on the vertical axis but makes use of rest-frame $U - B$ color rather than stellar mass (Yan et al. 2011, hereafter Y11). We display the AGN and star-forming fractions on this color-excitation diagram from Y11 in a similar fashion as for the MEx diagram [Figure 5(c,d)]. The original dividing lines are adapted from Y11 (straight lines) and the definition is included here for completeness:

$$\log([\text{O III}] \lambda 5007 / \text{H}\beta) = \max\{1.4 - 1.2(U - B), -0.1\}. \quad (3)$$

In this paper, we add a curve on the diagram from Y11 that follows the transition where the AGN probability is $P(AGN) > 30\%$. The new region between this curve and the straight lines is analogous to the MEx-intermediate region of the MEx diagram and contains $> 50\%$ of BPT-composite galaxies. The lower curve in Figure 5(c,d) is defined by:

$$y = 12.3914 - 27.0954x + 18.5122x^2 - 4.02369x^3, \quad (4)$$

where $y \equiv \log([\text{O III}] \lambda 5007 / \text{H}\beta)$ and $x \equiv (U - B)_0$. As in Y11, we calculate the rest-frame $U - B$ color, expressed in AB magnitudes, by using the *k-correct* v4.1.4 code from Blanton & Roweis (2007).

The bivariate distributions of galaxies on both the mass-excitation (MEx) and the color-excitation (CEX) diagrams are examined in more detail in Appendix A.

The SDSS subsample used here has been implemented as a reference to provide probabilities of each class as a function of the location on the MEx (or CEX) diagram. Given a stellar mass and $[\text{O III}] \lambda 5007 / \text{H}\beta$ ratio, our publicly available IDL⁴ routines⁵ return a probability that the input galaxy belongs to the SF, composite, LINER, and Seyfert 2 categories. The MEx diagram is well motivated from the successes at separating and quantifying the overlap of BPT-classes for a large SDSS sample of galaxies. We will apply this new diagnostic to a sample

of galaxies at $0.3 < z < 1$ in the following sections.

4. INTERMEDIATE-REDSHIFT GALAXY SAMPLE

Our intermediate-redshift galaxy sample is based on observations from the Great Observatories Origins Deep Survey⁶ (GOODS) and the All-wavelength Extended Groth strip International Survey⁷ (AEGIS). Most of the analysis is performed on galaxies at $0.3 < z < 1$, although we extend the range to slightly lower values when we use redder emission lines (such as in §5.1).

Optical spectra are drawn from the Team Keck Redshift Survey⁸ (TKRS Wirth et al. 2004) for galaxies in the GOODS-North (GOODS-N) field, and from the DEEP2 Galaxy Redshift Survey (hereafter DEEP2; Davis et al. 2003, 2007) for galaxies in the Extended Groth Strip (EGS) field. These two spectroscopic surveys have similar limiting magnitudes of $R_{AB} = 24.3$ and 24.1, respectively. The former lies within GOODS-N ($10' \times 16'$) and includes redshifts for 1440 galaxies (1044 galaxies with confident redshifts $0.3 < z < 1$). From the DEEP2 survey, we only use the pointing in the Extended Groth Strip (centered at 14 17, +52 30) covering $120' \times 15'$. There are 6,588 DEEP2 galaxies with confident redshifts $0.3 < z < 1$ in this pointing.

Both sets of observations were obtained with the DEIMOS spectrograph (Faber et al. 2003) at the Keck Observatory and reduced with the pipeline⁹ developed by the DEEP2 team at the University of California-Berkeley. However, their spectral resolution and spectral range differ due to the use of different gratings (600 line mm^{-1} for TKRS and 1200 line mm^{-1} for DEEP2). The TKRS resolution is 4\AA full-width-half-maximum (FWHM) over the wavelength range 5500–9800Å, whereas DEEP2 spectra have a resolution of 2\AA FWHM with a wavelength coverage of 6500–9100Å. These different spectral ranges mean that emission lines of interest are accessible over somewhat different redshift ranges for the two samples. $\text{H}\beta$ and $[\text{O III}] \lambda 5007$ can be observed out to $z \sim 1$ with TKRS spectra but only out to $z \sim 0.8$ with DEEP2 spectra.

A wealth of multiwavelength data is available in both GOODS-N and EGS. In this paper, we utilize ancillary *Chandra* X-ray data, *Spitzer* IRAC data, and ground-based optical imaging (§4.2). *Spitzer*/IRAC photometry is available in all four channels (available through the *Spitzer* Science Center, also see Barmby et al. 2008, for EGS). In what follows, IRAC photometry is used to estimate the rest-frame K -band magnitude (§4.2). We take advantage of the fact that the *Chandra* X-ray coverage is very deep: 2 Msec in GOODS-N (Alexander et al. 2003) and 200 ksec in EGS (Laird et al. 2009; Nandra et al. 2005). This provides us with an independent AGN/star-forming classification scheme (§5). The sensitivity of the shallower data is adequate to ensure the detection of luminous X-ray sources ($L_{2-10\text{keV}} > 10^{42} \text{ erg s}^{-1}$, a nominal luminosity threshold for AGN) out to $z \sim 1$. Furthermore, we can detect fainter X-ray galaxies (including starbursts) at all redshifts in GOODS-N.

⁶ <http://www.stsci.edu/science/goods/>

⁷ <http://aegis.ucolick.org/>

⁸ <http://tkserver.keck.hawaii.edu/tksurvey/>

⁹ <http://astro.berkeley.edu/~cooper/deep/spec2d/>

⁴ Interactive Data Language.

⁵ <http://monkey.as.arizona.edu/~sjuneau/AGN-Galaxy-Classification.html>

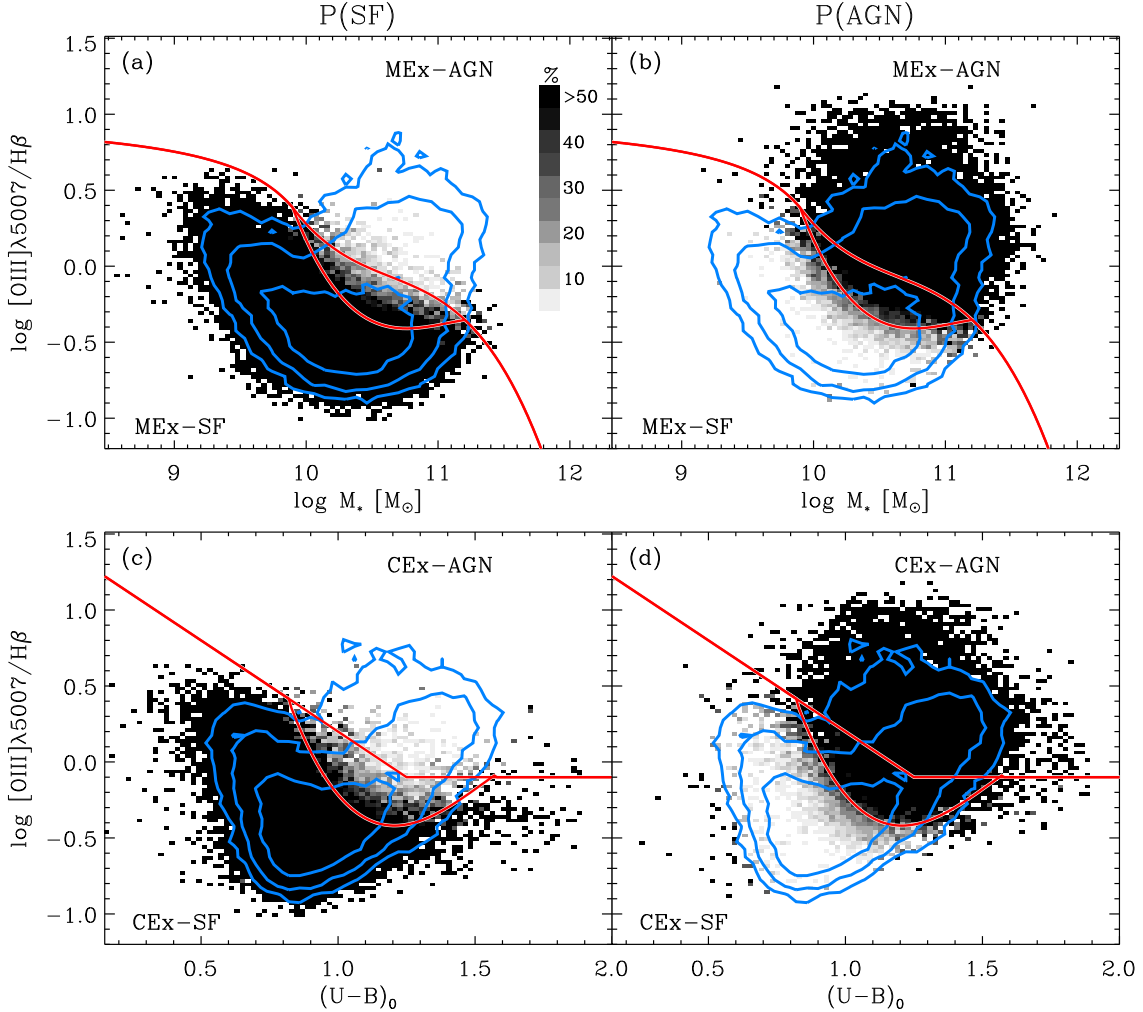


FIG. 5.— Percentages of galaxies classified as star-forming or AGN (all sub-categories) as a function of location on the MEx and CEx diagrams (top and bottom row, respectively). The left-hand side shows the number of SF galaxies divided by total number galaxies, or $P(SF)$, in each bin ($0.04 \text{ dex} \times 0.04 \text{ dex}$) for the MEx (a) and CEx (c) diagrams. The AGN percentages $P(AGN)$ are displayed on the right hand side, where panel (b) is the MEx diagram and panel (d) the CEx diagram developed by Y11. $(U - B)_0$ denotes the rest-frame $U - B$ color expressed in AB magnitudes. In all panels, the upper lines mark the main division between AGN and star-forming galaxies, whereas the lower lines approximately correspond to a transition from $P(AGN) < 30\%$ (below) to $P(AGN) > 30\%$ (above). Galaxies between both sets of lines are a mixed SF/composite population, which we call MEx-intermediate galaxies (or CEx-intermediate in panels c,d). The bivariate distribution of the SDSS sample combining all galaxy classes is shown with logarithmic contours. (A color version of this figure is available in the online journal.)

4.1. Emission Line Fluxes

Emission line fluxes from the TKRS and DEEP2 spectra were measured using automated IDL routines. For each emission line, we fit the continuum with a linear relation over 30 \AA windows on either side of the line with a biweighting scheme. This technique efficiently rejects outliers and is thus robust against pixels with large errors (e.g., due to large sky subtraction residuals). If the flux density at the line peak is greater than three times the standard deviation of the continuum, the line is fitted with a Gaussian function. In such cases, we calculate emission line fluxes in two ways. First, we integrate the resulting Gaussian fit over a wavelength range corresponding to $\pm 2.5\sigma$, where σ is the Gaussian width parameter ($= \text{FWHM}/2.35$). Secondly, we directly integrate the continuum-subtracted spectra over the same wavelength range.

In most cases, we use the fluxes obtained from integrating the data directly. However, some potentially problematic cases were flagged for visual inspection. Among 509 TKRS galaxies for which both the $H\beta$ and $[\text{O III}] \lambda 5007$ emission lines passed the signal-to-noise and quality criteria, 61 were flagged as uncertain. Similarly, 245 among 2,536 DEEP2 galaxies were flagged for visual inspection. This generally occurs when the data are corrupted nearby the targeted emission line, or when the Gaussian fit is inadequate. These objects are examined on a case-by-case basis, and the flux measurement is adjusted accordingly. Among a total of 306 galaxies that were examined, 184 were validated whereas 122 were flagged as uncertain and not used in subsequent analysis.

We correct for underlying stellar absorption at $H\beta$ and $H\alpha$. TKRS spectra with a median signal-to-noise ratio (S/N) per pixel greater than three were fit individually using Bruzual & Charlot (2003, hereafter BC03) spectral

synthesis models. Utilizing IDL *simplefit* routines (C. Tremonti, private communication), we fit the continuum of the galaxies with a linear combination of ten representative stellar population templates, leaving dust obscuration as a free parameter. We subtract the continuum to correct Balmer lines for underlying stellar absorption. The median corrections (\pm half of $84^{\text{th}} - 16^{\text{th}}$ percentile range), expressed in terms of equivalent widths (EWs), are $2.8(\pm 0.9)$ Å at H β and $1.4(\pm 0.7)$ Å at H α . These values were applied to spectra that were not fit individually due to low signal-to-noise ratio or uncertain spectrophotometry. We note that applying the median correction to H β (H α) for spectra with an individual fit changes their line fluxes by 0.08 (0.03) dex r.m.s.

In addition to using line ratios, we will use [O III] $\lambda 5007$ luminosities to quantify the strength of AGN activity (e.g., in §6). For that purpose, the slit loss corrections are obtained by calculating synthetic photometry from the spectra in the band nearest to the observed wavelength of [O III] $\lambda 5007$ (usually ACS *F775w* or *F814w* for GOODS-N and EGS observations, respectively) and comparing to the true observed photometry. The synthetic photometry is obtained by applying the filter curve and integrating over the wavelength range of interest in the observed band. The ratio between the total flux from observed photometry and the synthetic photometry is used as a multiplicative correction factor. The median slit loss correction is a factor of two.

4.2. Stellar Masses

The stellar masses of our intermediate-redshift sample were calculated by fitting stellar population synthesis models to spectral energy distributions (SEDs) measured by galaxy photometry. The procedure is described in Salim et al. (2007). For galaxies in EGS, the following photometric bandpasses are used: FUV, NUV (GALEX), *ugriz* (CFHTLS), and *K* (Palomar) (see Salim et al. 2009; Gwyn 2008, 2011; Bundy et al. 2006). For galaxies outside of the Canada-France-Hawaii Telescope Legacy Survey (CFHTLS) field-of-view, we use CFHT 12k *BRI* photometry from Coil et al. (2004). For GOODS-N, the constraints are provided by the following photometry: *UBVRIz* taken from Capak et al. (2004) and *JK* obtained with the Flamingos camera on the Mayall 4 m NOAO telescope. In GOODS-N, the SED fitting is performed for galaxies with $K < 20.5$ (Vega) (as in Daddi et al. 2007, but extending to lower redshifts).

The calculations assumed a Chabrier IMF (Chabrier 2003), and output a probability distribution function (PDF) for the stellar mass. We assume the average of the PDF as the stellar mass, and estimate errors from the 2.5th and 97.5th percentiles [= $(97.5PL - 2.5PL)/3.92$]. Note that this fitting method is highly uncertain for systems with a Type 1 AGN (identified by broad emission lines arising from the broad-line region) for which the central engine may contribute enough photons to affect the broad-band photometry and alter the SED fitting results. However, these broad-line AGNs are easily identified and are not the object of this study, which targets narrow-line objects (Type 2 AGNs, LINERs, and star-forming galaxies).

We note that, for SDSS galaxies, the method used by Salim and collaborators to derive stellar masses was

tested against the results from Kauffmann et al. (2003). Salim et al. (2005) found a very good agreement between the two distinct methods and calculated the scatter of the difference to be 0.11 dex (without 3σ outliers, see their Fig. 1), which is smaller than the typical uncertainties for our galaxy sample. Thus, we do not anticipate strong systematic differences to be associated with the methods used to derive stellar masses for the low-redshift and intermediate-redshift samples that we use.

In general, we find that the values of stellar mass correlate well with the absolute rest-frame *K*-band magnitudes (M_K). The latter are obtained by applying a *k*-correction to the observed IRAC $3.6\mu\text{m}$ photometry. We calibrate the relation between M_* and M_K (see Appendix B) for galaxies with both of these estimates in order to estimate a stellar mass for galaxies lacking SED fitting calculations.

Starting from 2,561 galaxies with a valid stellar mass from SED fitting ($\chi^2 < 7$) and satisfying our emission-line selection, we augment our sample with 251 stellar masses estimated from M_K . The added galaxies had either missing photometry or an unacceptable SED fit ($\chi^2 > 7$). We obtain a total sample size of 2,812 galaxies at $0.3 < z < 1$ with stellar mass estimates and valid [O III] $\lambda 5007$ and H β emission line fluxes.

4.3. X-ray Luminosity and Classification

We convert X-ray fluxes in the hard band (2 – 8 keV; rest-frame 2.6 – 16.0 keV at $z = 0.3 - 1$) to rest-frame 2 – 10 keV luminosities, assuming a power-law spectrum with photon index as calculated in Alexander et al. (2003) to perform the *k*-correction. The fluxes are corrected for Galactic extinction but not for absorption intrinsic to each galaxy.

Our X-ray classification is based on two criteria: (i) $L_{2-10\text{keV}} > 10^{42}$ erg s $^{-1}$; (ii) hardness ratio¹⁰ $HR > 0.1$ (which corresponds to photon index $\Gamma < 1$). X-ray sources are classified as AGN if they satisfy *at least one* of these criteria. Otherwise, they are classified as X-ray starbursts. We cannot rule out that some AGNs may fail both the luminosity and hardness criteria due to X-ray absorption or intrinsically weak emission. Those objects are especially interesting in the framework of this study given the difficulty in identifying them using solely X-ray observations. We keep this possibility in mind as we will look for AGN signatures at other wavelengths besides X-rays.

Some galaxies lack a detection in the hard band (2 – 8 keV) but are detected in the full band (0.5 – 8 keV). In these cases, we *k*-correct the full band fluxes to obtain rest-frame 2 – 10 keV luminosities assuming an index $\Gamma = 1.9$. These galaxies will be marked with different plotting symbols when using their inferred $L_{2-10\text{keV}}$ since those values may be limits.

Formally, our classification scheme differs from that described in Bauer et al. (2004). Those authors used a different X-ray luminosity threshold ($L_{0.5-8\text{keV}} > 3 \times 10^{42}$ erg s $^{-1}$) and also included criteria based on inferred Hydrogen column density and the presence of broad (> 1000 km s $^{-1}$) or high-ionization emission lines in the optical spectrum. Here, we aim for a classification

¹⁰ Hardness ratio $\equiv (H-S)/(H+S)$, where H and S are the number of X-ray counts in the hard (2-8 keV) and soft (0.5-2 keV) bands.

based only on X-rays, independent from optical spectroscopy. Nevertheless, we note that the resulting classification is very similar for galaxies that overlap between the sample from Bauer et al. (2004) and that presented here.

We consider X-ray detections for most of our analysis but we also calculated X-ray upper limits for GOODS-N galaxies that were selected based on their [O III] $\lambda 5007$ luminosity. The X-ray upper limits were calculated following §3.4.1 of Alexander et al. (2003) and assuming $\Gamma = 1.9$.

5. DIAGNOSTICS AT REDSHIFT 0.3 – 1

Now that we have calibrated the MEx diagram at low-redshift with SDSS galaxies, we apply it to a sample of intermediate redshift galaxies. Our sample, described in §4, contains 2,812 galaxies at $0.3 < z < 1$ from the GOODS-N and EGS fields with valid $H\beta$ and [O III] $\lambda 5007$ measurements.

5.1. Comparison with X-ray Classification

The validity of the MEx diagram was demonstrated by showing a good correspondence with the BPT classification in §3.1. Here we show another line of support based on the comparison of the MEx classification with a completely independent scheme based on X-ray observations. As can be seen in Figure 6(a), 85% (34/40) of the X-ray AGNs with valid emission line measurements ($S/N > 3$) are classified as MEx-AGN (26/40) or MEx-intermediate (8/40) on the MEx diagram. Thus the MEx diagram has a high success rate for recovering X-ray identified AGNs.

As for the X-ray starbursts, 50% (8/16) are classified as SF on our new diagram, while 19% (3/16) are in the intermediate region and the remaining 31% (5/16) reside in the AGN region. However, low-luminosity AGNs and some heavily absorbed AGNs may appear as faint as X-ray starbursts so this class of objects likely includes these different systems in addition to genuine starbursting galaxies. Indeed, the two X-ray starbursts that are in the AGN region of the MEx diagram but that lie at sufficiently low redshift to be placed on the BPT diagram ($z < 0.5$) stand out in the BPT-AGN region (Figure 7), further confirming the presence of actively accreting black holes in these galaxies. The optical diagnostics are thus especially useful when the X-ray signal alone is ambiguous (e.g., too faint to securely identify AGNs). Additional support for the presence of AGN in the X-ray starburst class is provided for at least one galaxy for which we have a clear detection of the [Ne V] $\lambda 3425$ emission line (Figure 8). This transition is an unambiguous tracer of AGN activity because of its high ionization potential (97.1 eV).

Next, we use the MEx classification probability method described in §3.3. We calculate $P(\text{AGN})$ by adding the probabilities of any AGN category (composite, LINER and Seyfert 2). We will show in §5.2 that $P(\text{AGN}) > 30\%$ is a useful threshold to distinguish AGNs from purely star-forming galaxies. When X-ray AGNs, X-ray starbursts, and non-X-ray detections are considered separately, we find that 29 among 35 X-AGNs (83%) galaxies have $P(\text{AGN}) > 30\%$, with an average AGN classification probability of 77%. For the X-ray starbursts, which all have a low hard X-ray luminosity ($L_{2-10\text{keV}} < 10^{42} \text{ erg s}^{-1}$), we find that 11 among 17 X-SBs (65%)

have $P(\text{AGN}) > 30\%$ (average $P(\text{AGN}) = 52\%$). This suggests that some of them host an X-ray absorbed or X-ray weak AGN. Lastly, we note that some of the galaxies lacking an X-ray detection lie well into the AGN region with $P(\text{AGN})$ up to 100%. These X-ray faint AGN candidates are studied in more detail in §5.2. Like the X-ray starburst class, they may in fact include weak or heavily absorbed AGNs.

Not all of the X-ray detected sources have valid emission line measurements. X-ray galaxies for which only one of $H\beta$ or [O III] $\lambda 5007$ is measured and the other line has an upper limit are shown in Figure 6(b). In these cases, the [O III]/ $H\beta$ line ratio is either an upper or lower limit. We find that most X-ray classified AGNs appear consistent with their optical classification given their limits on the MEx diagram. X-ray galaxies for which no lines could be measured due to insufficient data quality or intrinsic weakness of the emission lines are considered in §5.3.

We note that the locus of our intermediate-redshift star-forming galaxies may be offset slightly from the SDSS contours. A more careful analysis of the selection effects would be required to determine whether such a shift is real or simply results from selection biases. We discuss possible evolutionary effects in §7.5.

Overall, the MEx diagram is a new tool that can be used on galaxies with [O III] $\lambda 5007$ and $H\beta$ line fluxes as well as stellar mass. It is thus possible to apply a robust AGN diagnostic to optical spectroscopic samples out to $z \sim 1$, provided the galaxies also have photometry allowing a stellar mass estimate. An independent X-ray classification scheme supports the validity of our diagram. This means that surveys with optical spectroscopy but lacking X-ray coverage can still benefit from a reliable AGN diagnostic.

In order to complete the comparison between the optical MEx diagram AGN classification, and the X-ray based classification, we perform two experiments. First, we use X-ray stacking to search for AGN signatures in galaxies that are undetected in the X-ray observations (§5.2). Second, we calculate the demographics of all X-ray AGNs regardless of the presence of optical emission lines (§5.3). This exercise highlights the complementarity of the optical and X-ray selection techniques.

5.2. X-ray Stacking

Stacking the X-ray observations allows us to probe X-ray emission to fainter flux levels and, in the case of significant detections in more than one energy band, to estimate the X-ray spectral slope. The X-ray spectral slope (or photon index Γ) can be used to distinguish between different source types. While unabsorbed AGNs and low-mass X-ray binaries (LMXBs) exhibit a large index ($\Gamma > 1.3$ and > 1.7 , respectively), high-mass X-ray binaries (HMXBs) can yield flatter slopes with indices down to ($\Gamma > 0.5$) and absorbed AGNs have still flatter slopes with ($-1 < \Gamma < 1$). These ranges are illustrated on Figure 2 of Alexander et al. (2005, see references therein).

In the case of X-ray absorbed AGNs, the flattening is caused by the photoelectric absorption of soft X-ray photons by heavy atoms in neutral gas along the line of sight. Because softer photons are preferentially absorbed relative to harder ones, Compton-thick AGNs

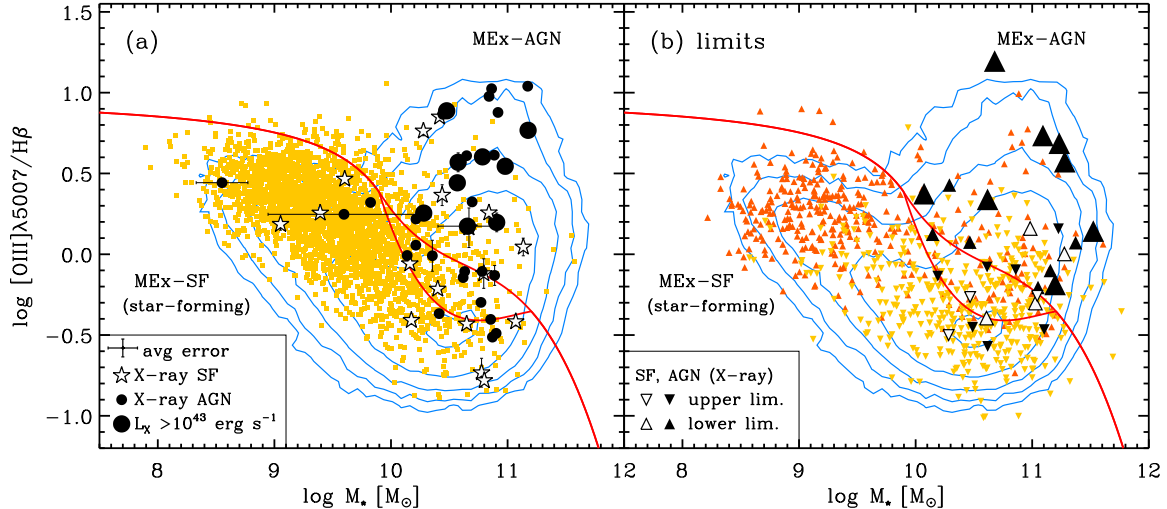


FIG. 6.— Application of the MEx diagnostic to identify the presence of active nuclear activity within galaxies at $0.3 < z < 1$. Contours show the SDSS low- z sample (evenly spaced on a logarithmic scale). (a) Our intermediate redshift sample is superimposed (filled squares) and, when available, the X-ray classification is marked with larger symbols [star symbols for X-ray starbursts; small (large) filled circles for X-ray AGNs with $L_X < 10^{43} \text{ erg s}^{-1}$ ($L_X > 10^{43} \text{ erg s}^{-1}$)]. We also show galaxies with only one emission line detection and one upper limit (b). The resulting $[O III] \lambda 5007 / H\beta$ ratios are upper limits when only $H\beta$ is detected (yellow downward triangles) or lower limits when only $[O III] \lambda 5007$ is detected (orange upward triangles). The X-ray classification is marked with open triangles for X-ray starburst, and solid black triangles for X-ray AGNs [small (large) for X-ray AGNs with $L_X < 10^{43} \text{ erg s}^{-1}$ ($L_X > 10^{43} \text{ erg s}^{-1}$)]. The empirical lines on the MEx diagram are described in the text (see §§3.1, 3.3). The error bar shown in the legend represents the typical uncertainty although we plot individual error bars for objects whose uncertainty are significantly larger. This diagram is applicable out to $z \sim 1$ and yields spectral classes that are very consistent with the independent X-ray classification shown here. (A color version of this figure is available in the online journal.)

(with $N_H > 10^{24} \text{ cm}^{-2}$) should exhibit a flat slope with $\Gamma < 1$. However there are at least two situations where Compton-thick AGNs instead have a steep X-ray slope at energies $< 10 \text{ keV}$. First, the shape of the X-ray spectrum varies greatly when the X-ray emission is dominated by reflection rather than direct transmission. In this case, the slope of the spectrum does not truly reflect the hardness of the radiation and one must use other indicators to estimate X-ray absorption (e.g., the equivalent width of the Fe $K\alpha$ line). Second, the photon index at energies $0.5 - 10 \text{ keV}$ can be significantly altered when soft emission from starburst activity is coincident with the harder emission from an absorbed AGN. We keep these possibilities in mind when we interpret the results of X-ray stacks.

In this paper, we perform two different X-ray stacking analyses. The first analysis is a proof-of-concept of the MEx diagram. In this case, the goal is to stack the X-ray signal for subsamples defined from the MEx classification. A more detailed description and the results are provided in this section. For the second analysis (described below in §6.3), we apply additional criteria to target specifically X-ray absorbed AGN candidates.

In this section, we are interested in galaxies that are not detected individually in the deep 2 Msec *Chandra* observations in GOODS-N but that have the required emission line measurements for the MEx diagram. Employing a stellar mass cut-off at $10^{10} M_\odot$ and requiring $H\beta$ and $[O III] \lambda 5007$ emission line detections ($S/N > 3$), there are 69 such galaxies at $0.3 < z < 1$.

For the X-ray stacking we adopt a similar approach to Worsley et al. (2005), who stacked sources and calculated the significance of the stacked result using 10,000 Monte Carlo trials. In all cases, we limit the X-ray stack-

ing to sources within 6 arcmin of the *Chandra* aim point to maximize sensitivity and we stack the sources in the soft and hard bands. Sources that lie within a factor of 2 of the 90% encircled energy radius of another X-ray detected source are excluded. We only consider the stacked signal as a significant detection when the number of detected counts in a given band exceed the background count rate determined from the Monte Carlo trials by $\geq 3 \sigma$.

Following the criteria outlined above there are 47 (out of 69) X-ray undetected galaxies in GOODS-N for which we can stack the *Chandra* data. We select subsamples of the X-ray undetected galaxies to stack based on the probabilities $P(AGN)$ & $P(SF)$. Here we use $P(AGN)$ as the total probability for the composite, LINER and Seyfert subclasses. We divide the sample at $P(AGN) > 50\%$ and also at $P(AGN) > 30\%$ in order to include the MEx-intermediate region.

In the former case, we find significant detections in *Chandra*'s soft band and marginal detections in the hard band for these $P(AGN) > 50\%$ and $P(SF) > 50\%$ subsamples of 25 and 22 galaxies, respectively. The X-ray spectral slopes are respectively flat ($\Gamma \sim 0.8$) and slightly steeper ($\Gamma \sim 1.2$; Table 2). A flat X-ray spectral slope of $\Gamma \sim 0.8$ unambiguously indicates the presence of absorbed AGN activity (see Fig. 2 of Alexander et al. 2005; Maiolino et al. 1998) in the $P(AGN) > 50\%$ subsample. The stacked signal of the complementary subsample may correspond to a mixture of star-forming galaxies and some absorbed AGNs. However, the difference in Γ between the $P(AGN) > 50\%$ and $P(SF) > 50\%$ subsamples is not statistically significant so there is a fair likelihood that some absorbed AGNs are present. This result suggests that $P(AGN) > 50\%$ may not be sufficient

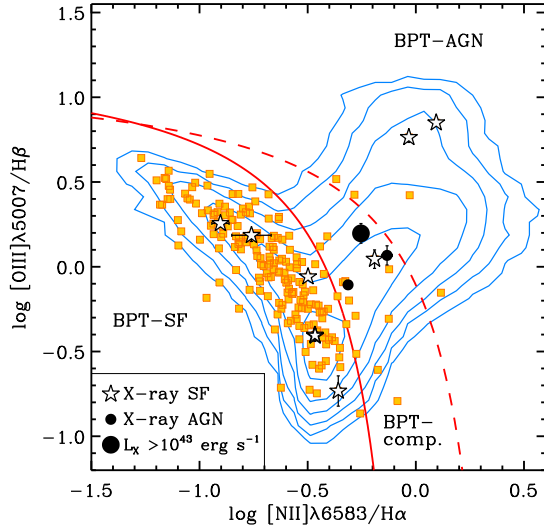


FIG. 7.— The BPT diagram, where BPT-AGNs are found above the dashed line (adapted from Kewley et al. 2001), star-forming (BPT-SF) galaxies below the solid line (adapted from Kauffmann et al. 2003), and composites (BPT-comp.) between the two lines. Contours show the SDSS low- z sample (evenly spaced on a logarithmic scale). The $z \sim 0.35$ galaxies for which we have all four diagnostic lines from TKRS ($0.2 < z < 0.5$) and DEEP2 ($0.3 < z < 0.4$) are mostly distributed along the star-forming sequence, with a few galaxies extending along the AGN plume (filled squares). We identify galaxies with a *Chandra* detection as a function of their X-ray classification [star symbols for X-ray starbursts; small (large) filled circles for X-ray AGNs with $L_X < 10^{43}$ ($L_X > 10^{43}$ erg s $^{-1}$)]. While all the X-ray identified AGNs lie above the Kauffmann line (solid line), there are also two galaxies nominally classified as X-ray starbursts that lie in the region where AGNs are prominent. These systems also lie in the MEx-AGN region [Figure 6(a)] and they may be X-ray weak or X-ray absorbed AGNs. In either case, the optical diagnostic is a useful complement to X-ray observations alone. (A color version of this figure is available in the online journal.)

to recover all of the AGNs.

Imposing a lower cutoff at $P(\text{AGN}) > 30\%$ yields 34 objects to stack. Stacking these sources gives significant detections in the soft and hard bands corresponding to a flat X-ray spectral slope of $\Gamma \sim 0.8$, again unambiguously indicating the presence of absorbed AGN activity. We then stacked the remaining 13 systems, with $P(\text{SF}) > 70\%$. In this case, we only find a significant detection in the soft band. The steep X-ray spectral slope ($\Gamma \sim 1.7$) is consistent with the X-ray emission of these galaxies being dominated by star formation processes. These analyses are summarized in Table 2 and provide good first-order confirmation that the combination of the MEx diagram and our probabilistic approach provides a comparatively clean selection of star-forming galaxies and AGNs.

Our results suggest that using $P(\text{AGN}) > 30\%$ as a threshold for nuclear activity leads to a cleaner separation between AGNs and star-forming galaxies than using $P(\text{AGN}) > 50\%$. We examine the objects with intermediate AGN likelihood separately by stacking the 12 galaxies with $30\% < P(\text{AGN}) < 50\%$. As expected, galaxies in this subset are likely composite systems. We calculate $P(\text{comp})$, $P(\text{LINER})$, $P(\text{Sy}2)$ separately and, on average, the composite class is 5.5 times more likely than the LINER and Seyfert 2 classes taken together. We find a flat spectral slope of $\Gamma \sim 0.6$, statistically indistinguishable from the $P(\text{AGN}) > 50\%$ subsample. This result in-

dicates that some galaxies with $30\% < P(\text{AGN}) < 50\%$ host an X-ray absorbed AGNs, therefore are an important population to search for Compton-thick AGNs and to take into account for a complete census of AGNs.

We have demonstrated that the MEx diagnostic diagram works well at intermediate redshift ($0.3 < z < 1$) given that the majority of the X-ray AGNs lie in the MEx-intermediate and MEx-AGN regions rather than the MEx-SF region. The X-ray stacking analyses presented in this section consolidate this result. Furthermore, there are unidentified AGNs within the X-SB class (nominally X-ray starburst although some sources with faint luminosities are more difficult to classify unambiguously) and within an X-ray undetected population. These can be identified using the MEx diagram.

5.3. Demographics of X-Ray Selected AGNs

So far, we have compared the X-ray and MEx classification schemes for galaxies with valid emission line measurements ($S/N > 3$ for $H\beta$ and/or $[\text{O III}] \lambda 5007$). Here, we also consider X-ray detected sources that have sufficient spectral coverage for both emission lines but nonetheless lack detections. We use the X-ray AGN classification described in §4.3 to keep only secure X-ray AGNs (i.e., with $L_{2-10\text{keV}} > 10^{42}$ erg s $^{-1}$ or hardness ratio $HR > -0.1$).

Combining GOODS-N and EGS subsamples, there are 101 X-ray detected AGNs with $H\beta$ and $[\text{O III}] \lambda 5007$ within the spectroscopic wavelength coverage. We require $S/N > 3$ for either $H\beta$ or $[\text{O III}] \lambda 5007$ in order to perform the MEx classification. Based on this criterion, 33% of the X-ray selected AGNs lack optical emission line signatures. Performing the MEx classification with the remaining 68 objects with emission line measurements shows that 60 are in the MEx-AGN or MEx-intermediate region, and the remaining 8 lie in the MEx-SF region. To summarize the demographics, 59% are in the MEx-AGN or MEx-intermediate regions (48% and 11%, respectively), 8% are in the star-forming region, and 33% lack a classification because their emission lines are either too weak or corrupted.

As a comparison, Y11 used an X-ray selected sample in EGS that is a superset of the EGS sample studied here. They combined DEEP2 spectra and MMT spectra that were obtained specifically to target X-ray sources that were not part of the DEEP2 slit masks (Coil et al. 2009). For their X-ray selected sample, they found that 51% met their AGN class based on the color-excitation diagram, 22% were in the star-forming region of their diagram and 25% lacked emission lines. Yan and collaborators refer to the latter as X-ray bright, optically-normal galaxies (XBONGs), which they study in more detail (also see Rigby et al. 2006; Trump et al. 2009).

A distinction between the present work and the results presented in Y11 is their lower signal-to-noise cutoff for emission line measurements ($S/N > 2$). We prefer to use a more conservative selection by imposing $S/N > 3$ based on the visual inspection of the spectra and the large residuals often present near the lines with $S/N < 3$. Allowing for a lower S/N is likely responsible for the apparent smaller fraction of galaxies lacking emission line measurements in Y11 although the difference between the two analyses is not statistically significant ($\sim 1\sigma$). We stress that using the intermediate region – where composite and star-forming galaxies overlap – helps to recover

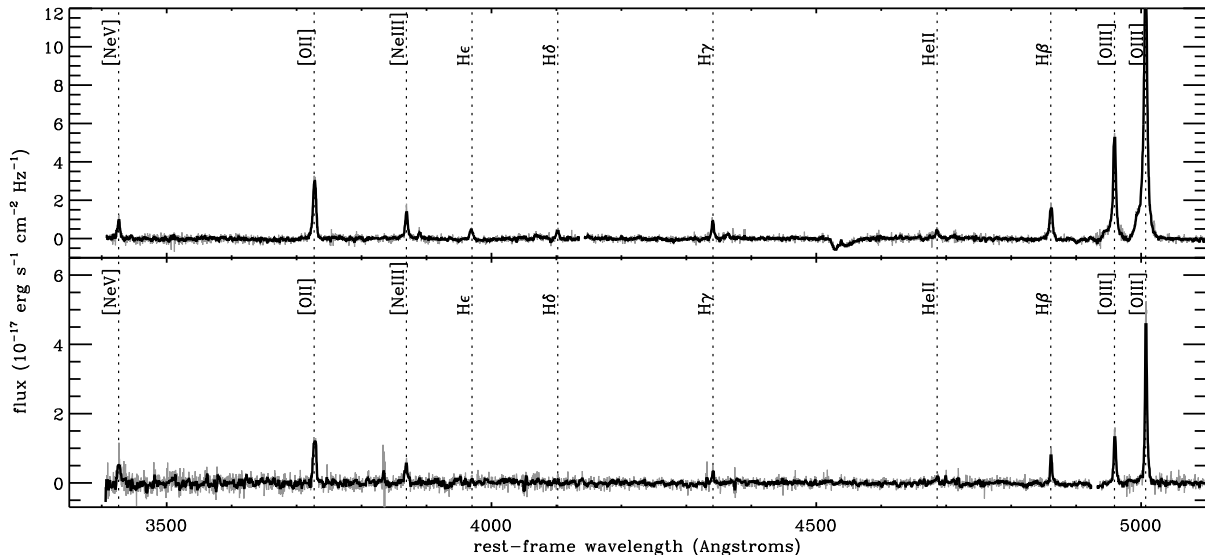


FIG. 8.— Two example TKRS spectra with the most obvious [Ne V] $\lambda 3425$ detections. While the top spectrum is for a galaxy that was also identified as AGN in the X-rays (J123608.13+621036.2, $z=0.679$), the bottom one is for a galaxy that was classified as X-ray starburst (J123645.40+621901.3, $z=0.455$). The spectra are continuum-subtracted (grey line) and smoothed with a running median (thicker black line). Typical emission lines are marked with vertical dotted lines and labeled.

a larger fraction of the X-ray detected AGNs, indicating the importance of composite systems in achieving a global AGN census.

In summary, we find that X-ray selected AGNs cover the full range of optical spectroscopic classes (AGN, SF, no or weak emission lines). Our results are similar to previous work. Also, we have shown that the MEx and X-ray AGN selection methods remain complementary. Some AGNs lack X-ray detection (or are X-ray faint) and we found evidence for absorption among that population. Given the importance of X-ray absorbed AGNs, and the possibility to start identifying this missing population, we will now focus on this topic.

6. COMPTON-THICK AGN CANDIDATES

While soft (0.5–2 keV) X-ray emission may be produced by star-formation activity, a large amount of hard (e.g., 2–10 keV) radiation is considered to be an obvious signature of AGN activity. However, large column densities ($N_H > 10^{24} \text{ cm}^{-2}$) can cause severe absorption even for hard X-rays, making it challenging to identify Compton-thick AGNs even with sensitive *Chandra* observations such as those used in this work.

In the event that photons with energies between 2–10 keV are absorbed by intervening material, it is possible to estimate the intrinsic luminosity of an AGN by looking at emission originating from larger scales than the source of absorption (e.g., Mulchaey et al. 1994; Bassani et al. 1999). Because [O III] $\lambda 5007$ emission arises in the narrow-line region, which extends several hundred parsecs beyond the active nucleus, it is not subject to the same small-scale nuclear absorption as hard (2–10 keV) radiation. This type of compact absorption is expected for geometries involving an obscuring torus as suggested in AGN unification models (Antonucci 1993). Thus, the ratio of X-ray (2–10 keV) to intrinsic (dust corrected) [O III] luminosities can serve as a Compton-thickness parameter T [$\equiv L(2\text{--}10 \text{ keV})/L([\text{O III}] \lambda 5007)$] (Bassani et al. 1999). This

quantity has two main caveats.

The first caveat is the uncertain obscuration of [O III] $\lambda 5007$ by dust in the host galaxy (external to the narrow line regions, Maiolino & Rieke 1995). For example, LaMassa et al. (2009) found a median correction of 1.0 mag (0.5 to 2.3 mag) at [O III] $\lambda 5007$ based on the Balmer decrement using a SDSS-selected sample of 17 Seyfert 2 galaxies that are [O III]-luminous. Given the uncertain dust obscuration corrections for [O III], we conservatively choose to use the observed luminosities in our analysis while keeping in mind that a typical correction of 1.0 mag would shift the values of the Compton-thickness parameter down by ~ 0.4 dex.

The second caveat is the possible contribution of stellar photoionization to the [O III] luminosity. Kauffmann et al. (2003) calculated the fractional contributions to emission line luminosities in galaxies hosting both star formation and AGN activity. For metal-rich galaxies with AGN, they found that only around 7% of [O III] $\lambda 5007$ luminosity is due to star formation (the remaining 93% originates from AGN-excited gas). This is in contrast with other lines such as H β and [O II] $\lambda 3727$ for which a larger contribution can be expected to come from H II regions rather than the narrow line region photoionised by the AGN (up to 45%–70%).

However, the stellar contribution to $L_{[\text{O III}]}$ can be much more significant in low-metallicity galaxies since oxygen becomes one of the main coolants and changes in line blanketing produce a harder ionization field (Kewley et al. 2006). To alleviate this source of contamination to the [O III] luminosity, we restrict the Compton-thickness analysis to high stellar mass (and presumably high-metallicity) galaxies, with $M_* > 10^{10.2} M_\odot$.

6.1. X-Ray Absorption Versus Observed AGN Power

In order to compare the X-ray absorption to the observed AGN power, we plot the Compton-thickness parameter T as a function of the observed (i.e., not corrected for absorption) hard X-ray luminosity (Figure 9).

Heckman et al. (2005) found that the average values of $\log(T)$ are 1.59 ± 0.48 dex and 0.57 ± 1.06 dex for Type 1 and Type 2 AGNs, respectively. Type 1s are less absorbed and show a tighter correlation while Type 2s include a much broader range of X-ray absorption (going down to smaller values of T). We reproduce this result in Figure 9(a) where we combine samples of Seyferts from Heckman et al. (2005) and Bassani et al. (1999). We also see a clear trend between the location of nearby Seyfert 2's on Figure 9(a) and their inferred column density N_H from Bassani et al. (1999). As expected, the Compton-thick galaxies, with $N_H > 10^{24} \text{ cm}^{-2}$, tend to lie at low values of T [$\log(T) \lesssim 0.25$ for observed X/[O III] ratios, and $\log(T) < -0.3$ after correcting $L_{[\text{O III}]}$ for dust obscuration].

Turning our attention to the sample of $0.3 < z < 1$ galaxies, we find a similar trend in X-ray absorption versus hard X-ray luminosity as found for the nearby galaxies. There is an apparent transition at $L_X \approx 10^{42} \text{ erg s}^{-1}$ (vertical dotted line). X-ray AGNs above that luminosity threshold span a restricted range in their X-to-[O III] luminosity ratio ($1 < \log(T) < 3$) compared to fainter hard X-ray sources. Galaxies that likely host an AGN based on the MEx diagram lie along the lower envelope of the distribution, consistent with their large [O III]/H β ratios being driven by luminous [O III] emission. Galaxies that are likely star forming according to the MEx diagram have lower X-ray luminosities on average, and occupy the mid-range of the Compton-thickness parameter values.

While some of the X-ray starbursts (open star symbols) were also classed as SF from the MEx diagram, there are a few objects with a conflicting spectral class. These X-ray-SB but MEx-AGN galaxies (open stars around red circles) are clustered around $\log(T) = 0$, the nominal value for Compton-thick AGNs. Given the predicted offset due to using uncorrected [O III] $\lambda 5007$ luminosities, and the location of known nearby Compton-thick AGNs on Fig. 9(a), we will adopt $\log(T) < 0.25$ as a criterion for identifying Compton-thick AGN candidates in the next sections. In cases with low values of $\log(T)$ the [O III] $\lambda 5007$ line luminosity may be a better indicator of the bolometric AGN luminosity. We investigate this next.

6.2. X-Ray Absorption Versus Intrinsic AGN Power

In the previous section, we considered candidate absorbed AGNs with a detection in the X-rays, at least in the full band. In this section, we will expand by including cases with upper limits in X-rays. Limits were derived for observations in GOODS-N as described in §4.3.

We again utilize the Compton-thickness parameter in Figure 10. Here, we use $L_{[\text{O III}]}$ on the horizontal axis to probe the intrinsic AGN power. Nearby [O III]-selected Seyfert 1's from Heckman et al. (2005) occupy the bright (elevated $L_{[\text{O III}]}$) and unabsorbed ($\log(T) > 1$) region of Figure 10(a). Seyfert 2's span a broad range of X-ray absorption and intrinsic AGN power.

In our intermediate-redshift sample (panel b), we note that star-forming galaxies seem to occupy a region contiguous with the Compton-thick candidates, which have $\log(L_{2-10\text{keV}})/\log(L_{[\text{O III}]}) < 0.25$. To discard these systems and keep absorbed AGN candidates, we select

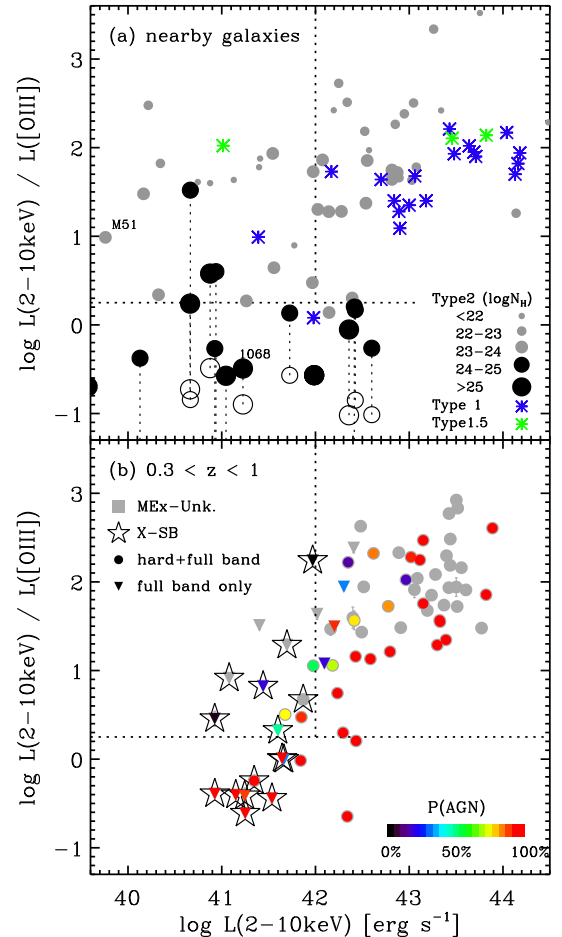


FIG. 9.— Compton-thickness parameter $T \equiv L_{2-10\text{keV}}/L_{[\text{O III}]}$ as a function of hard X-ray luminosity ($L_{2-10\text{keV}}$) for (a) nearby galaxies and (b) intermediate-redshift galaxies. In panel (a), the [O III]-selected type 1 AGN sample from Heckman et al. (2005) is shown with blue asterisks. Type 1.5 and type 2 AGNs (green asterisks and filled circles, respectively) are taken from Bassani et al. (1999). The symbols are keyed to the column density N_H in the case of type 2 AGNs (see legend). Dust-corrected [O III] values are shown with open circles for galaxies with $N_H > 10^{24} \text{ cm}^{-2}$. The intermediate-redshift sample (b) is selected to have $\log(M_*/[M_\odot]) > 10.2$, and is color-coded according to the probability to host an AGN from the MEx diagram (see color bar). The very likely AGNs (orange and red) tend to follow the bottom envelope of the points, and reveal some Compton-thick AGN candidates in galaxies that were otherwise classified as X-ray starbursts (star symbols; see §4.3). Most X-ray AGNs (points lacking star symbols) are characterized by $\log(L_X/L_{[\text{O III}]}) > 1$. Galaxies that were not identified on the MEx diagram (grey points) fail the emission-line quality flag for H β .

galaxies below the $L_X/L_{[\text{O III}]}$ threshold (red line) that also have a significant probability of hosting an AGN according to the MEx diagram. We adopt $P(\text{AGN}) > 30\%$ and stack the *Chandra* observations to search for hidden AGN signal in §6.3.

Figure 10 shows that the Compton-thick AGN candidates, with $\log(T) < 0.25$, span a similar range in [O III] $\lambda 5007$ luminosity as the unabsorbed AGNs, with $\log(T) > 1$. At high [O III] $\lambda 5007$ luminosities (e.g., $L_{[\text{O III}] \lambda 5007} > 10^{41} \text{ erg s}^{-1}$) the distribution of Compton-thickness values appears to be bimodal, with the AGNs being either largely unabsorbed ($\log(T) > 1$) or heavily absorbed ($\log(T) < 0.25$). We note that this possible bi-

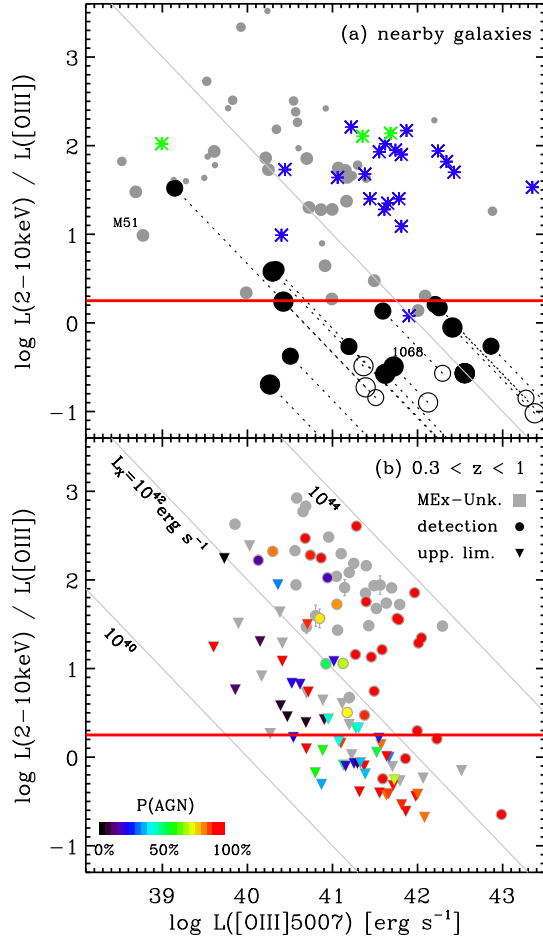


FIG. 10.— Compton-thickness parameter $T \equiv L_{2-10keV}/L_{[OIII]\lambda 5007}$ as a function of $[OIII]\lambda 5007$ luminosity. Both panels are shown on the same scale. Nearby galaxies are plotted in panel (a) and the symbols are as described in Fig. 9. The intermediate-redshift sample is shown in panel (b). The diagonal lines correspond to fixed hard X-ray (2 – 10 keV) luminosities of 10^{40} , 10^{42} , 10^{44} erg s^{-1} as labeled. We note that $L_{2-10keV} = 10^{42}$ erg s^{-1} is the nominal division that we adopt to separate X-ray AGNs from the X-ray starbursts although there are some X-AGNs below that luminosity threshold (recognized by their hardness ratio $HR > -0.1$). In addition to the X-ray classification, the MEx AGN probabilities are indicated with the color coding. $P(\text{AGN})$ includes all AGN classes, such that $P(\text{AGN})+P(\text{SF})=100\%$. Galaxies that were not identified on the MEx diagram (grey points) fail the emission-line quality flag for $H\beta$. This figure shows that star-forming/starburst galaxies occupy a contiguous region with the absorbed AGN candidates, stressing the importance of the MEx diagram in selecting likely AGNs. Based on the observed position of the known Compton-thick galaxies in panel (a), we adopt $\log(L_X/L_{[OIII]})=0.25$ as a criterion for Compton-thick candidates (horizontal line).

modality is seen in both the nearby and the intermediate-redshift galaxy samples. Our sample is mostly complete at the bright $[OIII]$ end¹¹ so we do not believe that this trend can be attributed to selection effects. However, the number statistics are too small to investigate it further.

Unsurprisingly given the fairly small volume probed, we mostly detect AGNs with Seyfert-like luminosities and below $[\log(L_{[OIII]}) < 42.5 \text{ erg s}^{-1}]$. However, we note two possible AGNs with intrinsic luminosity in the

¹¹ We detect galaxies with $L_{[OIII]\lambda 5007} > 10^{41} \text{ erg s}^{-1}$ out to $z = 0.95$

quasar regime [with $\log(L_{[OIII]}) > 42.5 \text{ erg s}^{-1}$], both of which appear to suffer from large X-ray absorption. These systems may be important testbeds for evolutionary scenarios where quasars are born in a deeply enshrouded environment (presumably following a major galaxy merger) before a blowout phase where the surrounding material is ejected revealing the optically and X-ray bright central engine (Sanders & Mirabel 1996; Di Matteo et al. 2005; Hopkins et al. 2005). We leave this analysis for future work.

In this section we have investigated the presence of X-ray absorbed AGNs by using both X-ray detected and X-ray undetected $[OIII]$ -selected objects. We find that the range of intrinsic luminosities probed by $L_{[OIII]}$ are comparable for Compton-thick candidates and X-ray unabsorbed systems. The presence of X-ray absorption is inferred from the X-to- $[OIII]$ luminosity ratio (T) and we utilize X-ray stacking analyses in the following section to further justify the presence of absorption in these systems.

6.3. X-ray Stacking of Highly-Absorbed AGNs

Here we search for X-ray signatures in the X-ray undetected absorbed AGNs with low X-ray/ $[OIII]$ ratios identified in the previous section (§6.2). There are 33 galaxies that are part of our candidate Compton-thick AGN selection¹² (see Fig. 10b). Sixteen are X-ray detected and are examined on a case-by-case basis below. Of the 17 X-ray undetected objects, 13 lie sufficiently close to the *Chandra* aim point without lying too close to X-ray bright sources to allow for X-ray stacking analyses. We employ the same X-ray stacking method described in §5.2. However, while in §5.2 we were concerned with stacking the X-ray data for galaxies selected solely from the MEx classification scheme, galaxies in this section are selected as potential Compton-thick AGNs by requiring $\log(T) < 0.25$.

Of the 16 X-ray detected sources, six are bright at X-ray energies ($F_{0.5-8keV} > 3 \times 10^{-16} \text{ ergs}^{-1} \text{ cm}^{-2}$) and ten are faint ($F_{0.5-8keV} < 3 \times 10^{-16} \text{ ergs}^{-1} \text{ cm}^{-2}$). The galaxies with bright X-ray fluxes tend to lie at lower redshift and have steep spectral slopes ($\Gamma \approx 1.3-2.0$). Two of the six X-ray bright sources have a clear $[\text{Ne V}] \lambda 3425$ detection (Fig. 8), an unambiguous tracer of AGN, and reside in the Seyfert 2 region of the BPT diagram. However, only one of them is clearly identified as an X-ray AGN ($L_X > 10^{42} \text{ ergs}^{-1}$; J123608.13+621036.2 in Fig. 8). This object is strongly absorbed ($\Gamma \sim 0.2$) and is a potential Compton-thick AGN. The remaining five X-ray bright sources fail both the luminosity and hardness criteria to be clearly identified as X-ray AGNs.

As for the X-ray faint galaxies, one is detected in the hard band and has a flat X-ray spectral slope ($\Gamma \approx 0.7$), indicating that it hosts a heavily absorbed AGN. The other nine objects are too faint to provide significant constraints on their X-ray spectral slopes. However, from stacking the *Chandra* data of these nine X-ray faint galaxies we find a comparatively steep X-ray spectral slope ($\Gamma \approx 1.4$), consistent with that found for the X-ray bright galaxies.

¹² $\log(L_{2-10keV})/\log(L_{[OIII]}) < 0.25$, $P(\text{AGN}) > 30\%$ and $\log(M_* [M_\odot]) > 10.2$.

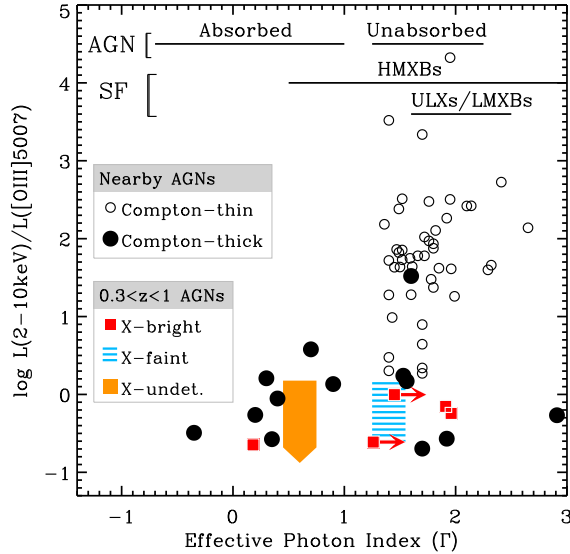


FIG. 11.— Compton-thickness parameter $T \equiv L_{2-10\text{keV}}/L_{[\text{OIII}]5000}$ as a function of the effective photon index (Γ) calculated as described in Bassani et al. (1999) and Alexander et al. (2003) for nearby and intermediate-redshift galaxies, respectively. The expected ranges of Γ are shown for various sources of X-ray emission at the top of the figure (taken from Alexander et al. 2005, and references therein). While Compton-thin galaxies have $\Gamma > 1$ as expected (open circles), Compton-thick AGNs can have either a flat or a steep index (filled circles; see text for details). We compare the locus of these nearby AGNs (open and filled circles) with the $0.3 < z < 1$ systems that we identified as Compton-thick AGN candidates based on the following criteria: $\log(T) < 0.25$, $P(\text{AGN}) > 30\%$ and $\log(M_\star/M_\odot) > 10.2$. The intermediate-redshift galaxies with bright X-ray fluxes (red squares) span a range of photon indices. One galaxy has an obviously flat slope ($\Gamma \sim 0.2$) and the remaining four have steeper slopes ($\Gamma > 1$) but are consistent with the range of values spanned by known, nearby Compton-thick AGNs (solid circles, from Bassani et al. 1999). We furthermore show the results from X-ray stacking of candidate Compton-thick AGNs that are either X-ray weak (light blue hatched region) or X-ray undetected (orange shaded region). The height of the shaded regions illustrates the range of values for the individual galaxies used in the stack (upper limits in the case of the non-detections). The sample of X-ray non-detections clearly includes absorbed AGNs. (A color version of this figure is available in the online journal.)

We stacked the *Chandra* data for the 13 X-ray undetected Compton-thick AGN candidates, which we treat separately from the individual detections. While the individually detected galaxies show steep X-ray indices, for the stacked objects we find a very flat photon index of $\Gamma \approx 0.4$ (see Table 2). The flatter slope found here strongly suggests the presence of X-ray absorbed AGN activity in at least a fraction of the objects that were stacked. The combined low X-ray photon index and small values of the thickness parameter make these systems robust Compton-thick AGN candidates.

Except for two objects, the results from the case-by-case analyses of the spectral slope are less obvious. The low X-ray-to-[O III] luminosity ratio and their position on the MEx diagram suggests that these X-ray detected objects host X-ray absorbed AGN activity, which may appear to be in conflict with the steep X-ray spectral slopes found for the majority of these systems. However, the steep X-ray spectral slopes do not preclude the possibility that all of these objects are heavily absorbed or Compton-thick AGN because the soft X-ray emission could be dominated by either scattered nuclear emission

or star formation (e.g., Matt et al. 2000). Indeed, known Compton-thick AGNs span a range of spectral slopes from very flat to very steep (Figure 11), encompassing the range that we observe in our intermediate-redshift sample. The nearby galaxies in Figure 11 are taken from Bassani et al. (1999) and divided between Compton-thin and Compton-thick at $N_H = 10^{24} \text{ cm}^{-2}$ (also see Figures 9 and 10). Overall, it is therefore possible that all of our Compton-thick AGN candidates are genuinely absorbed by Compton-thick material (colored symbols on Fig. 11); however, some of them cannot be unambiguously identified as such based on the X-ray slope alone. Higher energy observations ($> 10 \text{ keV}$) may help to confirm the presence of Compton-thick AGNs in galaxies with a steep X-ray slope.

6.4. Linking AGN Absorption and Optical Classification

Next, we show the X-ray absorbed AGN candidates on the MEx diagram in Figure 12(a). Interestingly, their location differs from that of the X-ray unabsorbed systems [Figure 12(b)]. The latter are distributed evenly in the main MEx-AGN region with a possible bias toward high stellar mass. In contrast, the absorbed AGN candidates cluster in the MEx-intermediate region with a few exceptions along the low-mass and outermost contour of the AGN plume. As a reminder, the MEx-intermediate region is populated by BPT-composites and BPT-SF galaxies. This suggests that the X-ray absorbed AGN candidates are more likely composite systems than Seyferts or LINERs.

While we consider all objects (X-ray detections and non-detections) together, we highlight the subset of 13 galaxies that were not individually detected but yielded a very flat X-ray spectral slope of $\Gamma \sim 0.4$ (see green squares on Fig. 12). The flat slope makes these systems robust Compton-thick AGN candidates. They occupy the MEx-intermediate region and the lower part of the AGN region where different AGN sub-classes overlap. The average probabilistic classification is $P(\text{AGN}) = 58\%$ with the AGNs three times more likely to belong to the composite sub-class than the Seyfert 2 and LINER sub-classes. This result strengthens our conclusion that composite galaxies, hosting both star formation and AGN, are a very important population to search for highly-absorbed AGNs. We further discuss these findings and their implications in §7.3.

7. DISCUSSION

Several previous studies have presented AGN diagnostic diagrams as alternatives to the BPT diagram. Because the $[\text{N II}] \lambda 6584/\text{H}\alpha$ line ratio is only available in optical spectra out to redshift ~ 0.4 , it needs to be replaced in order for the diagnostic to be applicable at higher redshift while avoiding the need to obtain near-infrared spectra. In this section, we first compare the MEx diagram with a few other AGN diagnostics from the literature (§7.1). We then discuss how the MEx diagram contributes toward a more complete census of AGNs (§7.2). We follow with a discussion of the importance of composite systems in this regard (§7.3) and we compare the fraction of absorbed AGNs from our work to results from the literature (§7.4). Finally, we mention possible evolutionary effects that are relevant to all nebular line diagnostic diagrams (§7.5).

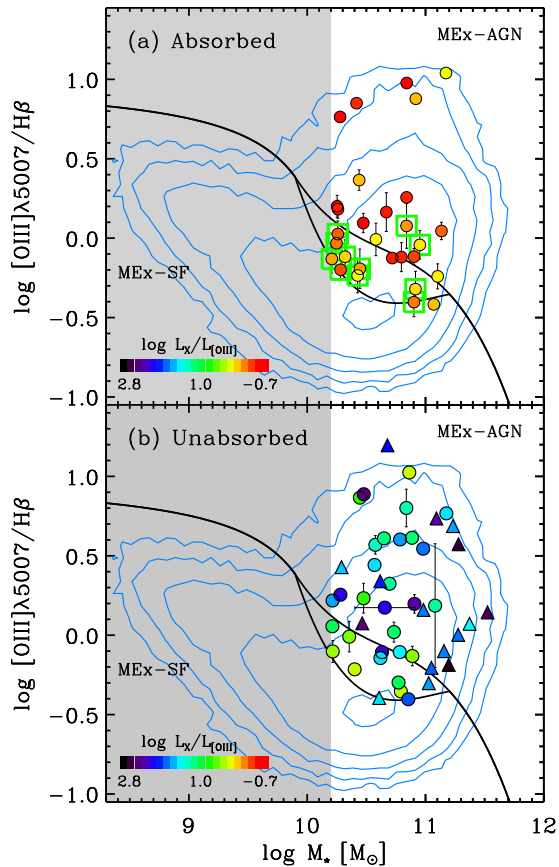


FIG. 12.— Systems with $P(\text{AGN}) > 30\%$ and $\log(M_* [M_\odot]) > 10.2$ shown on the MEx diagram. The points are color-coded according to the Compton-thickness parameter T shown in Figure 10. Red corresponds to the most absorbed systems, with $\log(T) \approx 0.7$ and the color changes gradually toward violet for the largest values of $\log(T)$ (≈ 2.8). Galaxies where both $\text{H}\beta$ and $[\text{O III}] \lambda 5007$ lines are robust detections ($S/N > 3$; filled circles) are shown in panels (a) and (b) depending if they are absorbed [$\log(T) \leq 0.25$] or largely unabsorbed [$\log(T) > 0.25$]. We also show galaxies with detected $[\text{O III}] \lambda 5007$ lines and $\text{H}\beta$ upper limits (triangles in panel b). In these cases, the $[\text{O III}] \lambda 5007/\text{H}\beta$ ratio is a lower limit. The green squares in panel (a) mark the X-ray undetected galaxies that yielded a flat spectral slope when stacked. Those tend to lie in the MEx-intermediate region indicating that some galaxies with a buried AGN are also undergoing an episode of active star formation.

7.1. Comparison with existing diagnostics

Lamareille et al. (2004) developed an AGN diagnostic diagram that, like the MEx diagram, is designed to be applicable to optical spectra of galaxies out to $z \sim 1$. In this case, the BPT diagram was modified by replacing the $[\text{N II}] \lambda 6584/\text{H}\alpha$ ratio with $[\text{O II}] \lambda 3727/\text{H}\beta$. Because of the greater wavelength separation between $[\text{O II}] \lambda 3727$ and $\text{H}\beta$, their flux ratio is very sensitive to dust obscuration. Thus, the authors opted for an equivalent width ratio to mitigate against that effect. The dividing lines on that diagram were recently revised (Lamareille 2010).

The so-called blue diagram (because it includes only blue lines compared to $\text{H}\alpha$) has the advantage of splitting the LINERs from the Seyfert 2s. However, it suffers from confusion between other classes of galaxies (SF, Sy2, and composites, see Lamareille et al 2004; Lamareille 2010; and Appendix C). The MEx diagram has a notably cleaner separation between SF and Sy2 galaxies, is

more sensitive to BPT-composite galaxies, and includes virtually all AGNs selected in the blue diagram.

In the case of the intermediate-redshift sample used here, a lot of galaxies with DEEP2 spectra have an insufficient wavelength coverage and do not contain all the lines required for the blue diagram. As a consequence, the number of galaxies for which we can use this diagram is much smaller than for the MEx diagram. The modest wavelength range required for the spectra makes the latter more versatile than the blue diagram, which requires $\Delta\lambda_{rest} > 2900 \text{ \AA}$.

For the galaxies that have all the required observations, we find that the X-ray AGN selection has a much better agreement with the MEx diagram (Appendix C). This seems to be partially due to the mixing between BPT-SF and BPT-Sy2 galaxies in one of the regions of the blue diagram, and the mixing between BPT-SF and BPT-composites in another region.

The approach most similar to the MEx diagram was developed by Weiner et al. (2007); in fact, those authors used datasets that overlap with the present study. They combined TKRS and DEEP2 spectra in order to benefit from both the larger wavelength coverage of TKRS and the larger number of galaxies in the DEEP2 survey. They investigated the trends between $[\text{N II}]/\text{H}\alpha$ and $[\text{O III}]/\text{H}\beta$ as a function of absolute H -band magnitude (M_H), and found that $[\text{N II}]/\text{H}\alpha$ was sufficiently correlated with M_H for the latter to be a helpful parameter when only the $[\text{O III}]$ and $\text{H}\beta$ lines are available. Weiner and collaborators did not go as far as developing a diagnostic line, but showed a division between the red and blue galaxies on those plots in the sense that the red galaxies are predominantly occupying the region where AGNs are expected to lie. This suggests that optical color may be another useful discriminant between star-forming and AGN galaxies when combined with $[\text{O III}]/\text{H}\beta$. Indeed, this approach was used recently by Yan et al. (2011).

Yan and collaborators designed a similar diagram as presented here, except for using rest-frame $U - B$ color in lieu of stellar mass. Their diagnostic produces comparable results to the MEx diagram when classifying the bulk of SDSS galaxies into AGN or star-forming. In detail, they chose to avoid targeting the composite galaxies that lie beyond the distribution of the more obvious AGNs (i.e., above the Kewley line in the BPT diagram). This implies that the galaxies on the star-forming side suffer from more frequent contamination by AGNs. Thus, we identified the region where the composite galaxies have an important overlap with star-forming galaxies (region between Eq. 3 and Eq. 4). The motivation is twofold. First, it provides a means to obtain a cleaner sample of star-forming galaxies. Secondly, we have shown that composite galaxies are an important population to look for highly-absorbed AGNs that are co-existing with star formation in their host galaxies. More detailed comparisons between the MEx diagram and the CEx diagram developed in Y11 are presented in §3.3 and Appendix A.

Another alternative diagram, called the DEW diagram, was developed by Stasińska et al. (2006). It includes a separation based on the 4000\AA -break and equivalent width of $[\text{Ne III}] \lambda 3869$ or $[\text{O II}] \lambda 3727$ (whichever is greater). In this case, the AGN hosts tend to have a larger $D_n(4000)$ with respect to normal star-forming

galaxies. Unfortunately, the 4000Å-break is located near, or directly over, the detector gap for most of the DEEP2 spectra at the redshift of interest (peaking near $z = 0.7$), so we are unable to apply this diagram for the bulk of our sample. The authors presented evidence that the DEW diagram has a better correspondence with the BPT diagram compared to the blue diagram (at least prior to its revision in 2010).

One notable difference between the MEx diagram and the original BPT diagram (or blue diagram) is that the former is not scale-free. The inclusion of stellar mass as a parameter imposes an absolute physical scale to the problem (whereas emission line ratios do not). This aspect raises questions about possible redshift evolution effects that could systematically affect the locus of the galaxies on diagnostic diagrams. We discuss such possibilities below (§7.5).

7.2. A More Complete Census of AGNs

Understanding active galactic nuclei and their role in galaxy evolution requires a robust AGN classification scheme. A complete sample should include both intrinsically weak and intrinsically bright but absorbed AGNs. Weak AGNs are interesting to study and learn more about the low accretion phase and whether the AGN unified model needs to be revised (Ho 2008; Trump et al. 2009). Absorbed AGNs are sought to explain the unresolved portion of the cosmic X-ray background, and to quantify their contribution to mid- and far-infrared emission seen in infrared-luminous galaxies. They are also of interest to test evolutionary scenarios where galaxy major mergers are invoked as a mechanism to form quasars, through a deeply-embedded and absorbed phase (Sanders et al. 1988; Fabian 1999; Hopkins et al. 2005).

The MEx diagram introduced in this paper is a tool to uncover AGNs that are weak in X-ray observations, presumably due to either intrinsic weakness or X-ray absorption. Both of these AGN phases – weak or absorbed – may be found in galaxies that are simultaneously undergoing episodes of star formation, potentially masking AGN signatures. One important feature that allows us to find these systems is our probabilistic approach.

As shown in §5.2, using $P(\text{AGN}) > 30\%$ as a threshold provides a more complete census of AGN than using $P(\text{AGN}) > 50\%$. We found that both high-probability AGNs ($P(\text{AGN}) > 50\%$) and medium-probability AGNs ($30\% < P(\text{AGN}) < 50\%$) that are not individually detected in the *Chandra* data show signs of X-ray absorption when we stacked their X-ray emission (from the resulting flat X-ray spectral slope; see Table 2). The galaxies with $30 < P(\text{AGN}) < 50\%$ are likely composite systems (see §5.2), and occupy a region of the diagram that overlaps with other classes, making them more challenging to identify without the probability approach. Thus, identifying those AGNs is a step toward a more complete census of active galactic nuclei.

Our finding that the X-ray undetected galaxies identified using the MEx diagram are likely absorbed AGNs prompted us to make a more systematic search for X-ray absorbed systems. We probed X-ray absorption using the Compton-thickness parameter T as described in §6.3 (see references therein). We again found a significant detection in *Chandra*'s hard band and a still flatter spectral slope ($\Gamma \approx 0.4$) for galaxies that were not detected

individually. This result supports the idea that the X-ray-to-[O III] luminosity ratio does select absorbed AGNs as expected. We also note some galaxies with a steep spectral slope ($\Gamma > 1$) and a low value of T . These systems are also consistent with X-ray absorption given that they are within the range of values of Γ and T spanned by known Compton-thick AGNs that are nearby and easier to study in more detail (see Fig. 11). In these cases, the soft X-ray emission may arise from a scattered AGN spectrum or from contamination by a superimposed starburst component.

To summarize the absorbed AGN samples, we first found signs of X-ray absorption in MEx-AGNs that were not detected at X-ray wavelengths. These samples were selected with no *a priori* knowledge of X-ray absorption and the results are tabulated in §5.2 (Table 2). We then specifically targeted X-ray absorbed AGN candidates by imposing $\log(L_{2-10\text{keV}}/L_{[\text{O III}]\lambda 5007}) < 0.25$ (§6.3). This yielded a sample of 33 absorbed AGN candidates: six have bright X-ray fluxes (and mostly a steep spectral slope, see red squares on Fig. 11); ten have faint X-ray fluxes and the stacked signal is characterized by a slightly steep slope (blue shaded region on Fig. 11), and of the remaining 17 that lack detections, 13 could be stacked and yielded a very flat spectral slope. So we have a sample of 33 candidates with heavy absorption of their X-ray emission, including a subsample of 15 more robust candidates (the 13 non-detections that were stacked plus the two individual detections that have a flat X-ray spectral slope).

7.3. Notes on Composite Galaxies

The separation between BPT-composites and BPT-AGNs is likely not as sharp as illustrated on the BPT diagram (Figure 1(a)) and may instead be a continuum of fractional AGN contribution to the spectral emission lines used in the diagnostic. This was suggested by, e.g., Kewley et al. (2006), who introduced a parameter to measure the distance from the star-forming sequence on the BPT diagram (also see Yuan et al. 2010). The AGN branches defined in Kewley et al. (2006) start from the metal-rich end of the star-forming sequence and follow mixing sequences toward larger values of $[\text{S II}]\lambda\lambda 6717, 6731/\text{H}\alpha$ or $[\text{O I}]\lambda 6300/\text{H}\alpha$ depending on the diagram used. The idea is that there is a continuous transition from star-forming toward AGN with an increasing AGN contribution.

Like composites, which host both star formation and AGN, galaxies classified as BPT-AGNs (above the Kewley line) may also have a significant star formation rate (SFR), up to $\sim 10 M_{\odot}\text{yr}^{-1}$ (Salim et al. 2007). On average their SFRs will be less than that in the population of composite galaxies (Salim et al. 2007). One consequence is that the emission lines of the BPT-composites are characterized by a smaller fractional contribution from AGN relative to star formation, which makes the line ratios more ambiguous. These results also imply a continuity (or mixing sequence) between star-formation and AGN-dominated systems. The so-called composites may be in the midst of a transition between the two types.

We might expect that some X-ray absorbed AGNs would reside in BPT-composite galaxies because large amounts of gas can provide fuel for star formation and act as absorbing material that attenuate X-ray signa-

tures. In this case the X-ray absorption could come from the host galaxy’s ISM in addition to torus-scale absorption. In addition, if the gas is also mixed with dust, or if the galaxy is viewed through a dust lane, AGN emission-line signatures such as [O III] $\lambda 5007$ can be weakened and further diluted with emission from peripheral star formation (Maiolino & Rieke 1995; Malkan et al. 1998; Goulding & Alexander 2009), causing the global signal to exhibit composite signatures.

The degree to which the host galaxy ISM absorbs X-ray and [O III] emission may vary depending on the detailed geometry of the emitting and absorbing regions. The X-ray emission arises on the very small scales of the accretion disk, while [O III] is emitted on the larger scale of the narrow line regions (reaching several hundred parsecs to kiloparsecs from the nucleus). If the absorption from the host galaxy ISM were approximated as a uniform screen with an extent that covers both the X-ray and narrow line emitting regions and with a Milky Way-like dust-to-gas ratio, then we would expect optical AGN signatures (such as [O III] $\lambda 5007$) to be obscured more than the X-ray emission. An extinction of $A_V = 10$ mag would fully obscure [O III] emission from the narrow line regions, but would correspond to a gas column density of $N_H = 1.6 \times 10^{22} \text{ cm}^{-2}$, causing only modest absorption of the X-ray emission. This would suppress the $L_{[\text{O III}]} / L_{2-10 \text{ keV}}$ ratio, leading to the opposite effect of the preferential X-ray absorption that we observe in some systems.

However, if the foreground ISM is clumpy, then it is possible for a dense cloud with large N_H to obscure the compact X-ray emitting region, while the average absorption to the larger [O III]-emitting narrow line regions could be much less. There will be lines of sight to the extended narrow line regions with more modest obscuration which will dominate the global emission line signal (relative to more heavily obscured lines of sight). As a result, we may in this case expect a preferential absorption of the X-ray emission relative to the optical ([O III] $\lambda 5007$) emission.

The preferential extinction of the small-scale X-ray emission when compared to the larger scale [O III] emission could also be caused by a physical connection between the gas at galaxy scales and the gas on the scales of the AGN torus. For example, in the simulations of Hopkins & Quataert (2010), an overall larger gas fraction on kpc scale can result in more gas funneling to the inner sub-pc region of the systems. These simulations predict that the transport of gas toward the central region depends most strongly on the disk-to-bulge ratio and on the gas fractions on 100 – 300 pc scales. We note that these authors did not specifically model a torus. However, the presence of instabilities on small scales increases the gas flow to the inner regions and suggests that the torus, often thought to be an extension of the accretion disk, could contain more obscuring material (or have a larger filling factor). If this scenario were true, it would imply that a higher gas fraction on galaxy scales could lead to both a larger SFR and a more gas-rich accretion disk (and potentially torus), thus creating preferential absorption of small scale emission (hard X-rays) relative to larger scale emission ([O III] $\lambda 5007$).

Based on these scenarios, and on our observations of a hard X-ray signal by stacking only 12 likely composite

galaxies (with $30 < P(\text{AGN}) < 50\%$, §6.3) that were not detected with very sensitive *Chandra* observations, we propose that not all BPT-composite galaxies have intrinsically weak *transition* AGNs. Instead, a fraction of them have powerful but absorbed AGNs whose light is diluted with that of their host galaxies (regardless of whether the host galaxy ISM provides additional AGN absorption or not).

In addition, the composite galaxy populations may differ with redshift. In general, star-forming galaxies had a higher specific star formation rate ($\text{SSFR} \equiv \text{SFR}/M_*$) at earlier times (Noeske et al. 2007; Elbaz et al. 2007). The larger amount of star formation at higher redshift is also linked to larger reservoirs of molecular gas (e.g., Daddi et al. 2010; Tacconi et al. 2010). As mentioned before, large amounts of gas contribute to increase the column density along the line of sight thus X-ray absorption. The more sizable gas reservoirs in isolated galaxies at higher redshift may be a way to obtain more absorbed AGNs without major mergers.

There is also evidence for a larger infrared-to-X-ray luminosity ratio with increasing redshift (Mullaney et al. 2010), further suggesting a larger SSFR in the host galaxies of higher-redshift AGNs relative to the current epoch. The enhanced star formation may affect the line ratios in the sense that more galaxies will be classified as BPT-composites at higher redshift. While we do not study star formation rates in this work, we remind the reader that the composite galaxy population plays an important role in the search for X-ray absorbed AGNs and as such should be identifiable at high-redshift. Thus, the MEX diagram and the probabilistic classification scheme introduced in this Paper are expected to fulfill this need and to contribute to a significant improvement in identifying the population of missing Compton-thick AGNs.

7.4. Absorbed AGN Fractions

Next, we examine the absorbed AGN fraction in terms of the number of galaxies identified as well as fractional contribution to $L_{[\text{O III}]}$. Galaxies with $\log(L_X/L_{[\text{O III}]}) > 1$ are considered as unabsorbed while galaxies with $\log(L_X/L_{[\text{O III}]}) < 0.25$ are considered absorbed and likely Compton-thick and galaxies in between are likely absorbed but Compton-thin with $22 < \log(N_H[\text{cm}^{-2}]) < 24$ [Figure 9(a)].

For galaxies in EGS, we compute X-ray upper limits using sensitivity and exposure time maps¹³. We convert the count rates in the hard band to fluxes assuming the conversion factor used by Laird et al. (2009). The X-ray detection limit is highly variable across the EGS field. For the [O III]-selected samples that we consider here, it varies from 6.6×10^{-16} to $1.2 \times 10^{-14} \text{ erg s}^{-1} \text{ cm}^{-2}$. The average value is $2.5 \times 10^{-15} \text{ erg s}^{-1}$, similar to the flux limit at which the survey is complete over 50% of the area ($2 \times 10^{-15} \text{ erg s}^{-1} \text{ cm}^{-2}$; Laird et al. 2009). We discard the X-ray upper limits of 10% (7/70) of [O III]-selected galaxies with $L_{[\text{O III}] \lambda 5007} > 10^{41} \text{ erg s}^{-1}$ because they lie in very shallow regions of the X-ray data (with upper limits that are $> 5 \times 10^{-15} \text{ erg s}^{-1} \text{ cm}^{-2}$).

However, we note that a typical upper limit value of $2.5 \times 10^{-15} \text{ erg s}^{-1} \text{ cm}^{-2}$ does not constrain the absorp-

¹³ Data products from <http://astro.ic.ac.uk/content/chandra-data-products>

tion very tightly, especially at $\log(L_{[\text{O III}]}) < 41.5$ where a lot of upper limits correspond to $\log(T) > 1$. Thus, we derive lower and upper limits to the absorbed AGN fraction by assuming that these galaxies are respectively all unabsorbed (i.e., they actually lie at $\log(T) > 1$) or all absorbed (i.e., they lie at $\log(T) < 1$). We furthermore weigh the galaxies with the probability that they host an AGN according to the MEx diagnostic. The fractional number and [O III] luminosity contribution of absorbed AGNs are respectively defined as follows:

$$f_{\text{absorbed}} = \frac{\sum_{i=1}^{N_{\text{absorbed}}} P(\text{AGN})_i}{\sum_{j=1}^{N_{\text{total}}} P(\text{AGN})_j} \quad (5)$$

$$f([\text{O III}]_{\text{absorbed}}) = \frac{\sum_{i=1}^{N_{\text{absorbed}}} P(\text{AGN})_i \times L([\text{O III}]_i)}{\sum_{j=1}^{N_{\text{total}}} P(\text{AGN})_j \times L([\text{O III}]_j)} \quad (6)$$

where $P(\text{AGN})$ is the fractional probability of hosting an AGN varying from 0 to 1, N_{absorbed} is the number of X-ray absorbed AGNs, and N_{total} is the total number of AGNs (absorbed and unabsorbed). At $\log(L_{[\text{O III}]}) > 41$, the absorbed (Compton-thick) fractions are poorly constrained: we find $f_{\text{absorbed}} = 25 - 81\%$ ($f_{\text{Compton-thick}} = 12 - 81\%$). Using equation 6, the fractional contribution of absorbed (Compton-thick) AGNs to the [O III] luminosity of all AGNs with $\log(L_{[\text{O III}]}) > 41$ is $f([\text{O III}]_{\text{absorbed}}) = 54 - 82\%$ ($31 - 82\%$).

The constraints are slightly better with a higher [O III] luminosity threshold. Restricting our analysis to the 34 galaxies at $0.5 < z < 0.8$ with $\log(L_{[\text{O III}]}) > 41.5$, we find an absorbed (Compton-thick) fraction ranging from 45% to 68% (17% to 68%) in number of galaxies, and a contribution to $L_{[\text{O III}]}$ between 70–81% (39–81%). Similarly, Y11 estimated an absorbed AGN fraction by calculating the X-ray detection probability assuming a constant intrinsic X-ray/[O III] $\lambda 5007$ ratio and measured [O III] luminosities, and by comparing the expected number of X-ray detections to the actual number of detections at the EGS depth. Attributing the non-detections to X-ray absorption, they find an X-ray absorbed fraction of $\sim 50-60\%$ at the same [O III] luminosity threshold used here, in agreement with our estimate for EGS and GOODS-N combined (45–68%).

Using only GOODS-N galaxies provides stronger constraints on X-ray absorption given the high sensitivity of the *Chandra* observations in that field, but is subject to smaller number statistics. In this case, restricting our analysis to the 29 galaxies at $0.3 < z < 0.8$ with $\log(L_{[\text{O III}]}) > 40.5$ yields an absorbed (Compton-thick) fraction of $75 \pm 18\%$ (54–64%). For $\log(L_{[\text{O III}]}) > 40.5$, Y11 calculated that 70.5% of AGN fail to be detected at the EGS depth, suggesting an absorbed fraction ($70.5 \pm 4.1\%$) that agrees with our calculations for GOODS-N galaxies (75%). Our results are also consistent with Akylas & Georgantopoulos (2009), who studied 38 nearby (< 70 Mpc) Seyferts and found an absorbed fraction $55 \pm 12\%$. Considering only sources with $L_{2-10\text{keV}} > 10^{41} \text{erg s}^{-1}$, they find that $75 \pm 19\%$ of 21 galaxies are absorbed ($N_H > 10^{22} \text{cm}^{-2}$) and 15–20% are Compton-thick.

At quasar-like luminosities, Vignali et al. (2010) found that 68% of SDSS Type 2 quasars at $0.3 < z < 0.8$ are

Compton-thick according to [O III] versus X-ray criteria. As they discuss, an [O III]-selection may bias the numbers toward a larger absorption fraction. Our estimates do not allow us to predict whether the absorbed AGN fraction rises or declines with [O III] luminosity. Larger samples with very sensitive X-ray observations would help to address that question.

7.5. Possible evolutionary effects

As noted in §5, there is some evidence that the intermediate-redshift galaxies may be offset in the MEx diagram relative to the lower-redshift SDSS sample. Other authors have reported similar shifts in the BPT diagram, i.e., higher- z galaxies appear displaced toward larger values of [O III]/H β and/or [N II]/H α . Some attributed this trend to varying HII region conditions (Liu et al. 2008; Brinchmann et al. 2008; Hainline et al. 2009) while others claim that additional AGN contribution may be the driving factor (Groves et al. 2006; Wright et al. 2010).

In particular, Wright et al. (2010) presented a detailed study of one BPT-composite galaxy at $z \sim 1.6$. Using adaptive optics combined with integrated field spectroscopy, they were able to separate the AGN from the host galaxy emission and found that the central region (inner $0.''2 \times 0.''2$) occupies the AGN part of the BPT diagram, while the integrated measurements place this galaxy in the BPT-composite region and the host galaxy alone shares the locus of the normal star-forming galaxies (i.e., not shifted from the low- z sequence). This suggests that diluted AGN contribution may explain the offset in at least some cases.

What would be the consequences of such offsets on the MEx diagram? If more galaxies have diluted AGN contributions, they will be selected as MEx-AGNs because the offset would tend to move the galaxies over the dividing line. A fraction of the higher-mass galaxies are already subject to be BPT-composite ($\sim 20 - 30\%$) so in this case, moving them over the AGN line would actually increase the completeness. On the other hand, if galaxies had different physical conditions in their HII regions in the past, in the sense of having larger [O III]/H β ratios compared to galaxies today, then some purely star-forming galaxies could be moved over the AGN dividing line. However, the differences out to $z \sim 1$ are probably small since the empirical offset is around 0.2 dex in $\log([\text{O III}]/\text{H}\beta)$.

Given that the situation is still under debate, and that selection effects are not well constrained, we do not implement an offset at this point. However, we note that the very good agreement between the X-ray and the MEx selection even out to redshift ~ 1 supports the conclusion that the empirical division works well over the redshift range considered here. Future work would be required to test whether it holds to even higher redshift.

8. SUMMARY

In this paper, we provide a new tool to gather a more complete census of actively accreting black holes in galaxies. We argue that intrinsically weak AGNs, as well as heavily absorbed AGNs, are important to understand the connection between supermassive black holes and their host galaxies. We successfully find systems that belong to these observationally-challenging AGN classes.

Using 110,205 emission-line galaxies from the SDSS, we calibrate a new excitation diagram to identify galaxy nuclear activity. By combining the observed $[\text{O III}] \lambda 5007/\text{H}\beta$ emission line ratio with stellar mass, we obtain a diagnostic applicable to galaxies out to $z \sim 1$. Here we summarize a few properties of the Mass-Excitation (MEx) diagram:

1. The simplest version splits galaxies into three classes: MEx-AGN, MEx-SF and MEx-intermediate. The latter is found in a region where BPT-composite galaxies have significant overlap with star-forming galaxies. The classification has an excellent correspondence to that from the BPT diagram based on $[\text{O III}] \lambda 5007/\text{H}\beta$ and $[\text{N II}] \lambda 6584/\text{H}\alpha$.
2. The classification scheme is refined using a novel probabilistic approach to predict the location of high-redshift galaxies on standard BPT diagrams based on their $[\text{O III}] \lambda 5007/\text{H}\beta$ ratio and stellar mass (§3.3). Utilizing SDSS priors, we calculate the probability of four mutually exclusive spectral classes (star-forming, composite, LINER, or Seyfert 2) as a function of position on the MEx diagram for each galaxy.
3. The MEx diagram offers a more complete AGN selection than alternatives such as the blue diagram (Lamareille 2010). It is comparable to the Color-Excitation (CEX) diagram developed by Yan et al. (2011) but may be particularly useful for dusty, strongly reddened galaxies which may have unusual colors. Furthermore, we add a dividing line to the CEX diagram to identify composite galaxies, an important population to search for absorbed AGNs.
4. We provide publicly available IDL routines to calculate the probabilities of different galaxy spectral classes based on the MEx and CEX diagrams.

Another outcome of a nearly complete AGN selection is that the complementary selection results in a very clean star-forming galaxy sample. Indeed, with our probability scheme, one can weight galaxies as a function of $P(\text{SF})$ when computing average properties such as the stellar mass-metallicity relation or the global star formation rate and thus mitigate against AGN contamination. We anticipate that a wide variety of applications will benefit from our approach to galaxy spectral classification.

We successfully classify AGN and star forming galaxies at $0.3 < z < 1$ using our new diagnostic. The sample is drawn from the AEGIS and GOODS-N surveys. Our main findings are as follows:

- An independent X-ray classification scheme shows that the MEx diagram selects around 82% of the X-ray AGNs with detected emission lines ($S/N > 3$ for $\text{H}\beta$ and $[\text{O III}] \lambda 5007$). When considering all X-ray AGNs, we find that 59% are in the MEx-AGN or MEx-intermediate regions, 8% are in the star-forming region, and 33% lack a classification (they fail the $S/N > 3$ requirement for valid emission line detections).

- The MEx diagram reveals X-ray absorbed AGN candidates, which were missed or mis-identified in X-rays while having robust signatures in their optical spectra. We combine support from three lines of evidence:

1. The subset of these galaxies with a low enough redshift to be placed on the BPT diagram lie in the BPT-composite or BPT-AGN regions (Fig. 7). In addition, one galaxy has a clear detection of $[\text{Ne V}] \lambda 3425$ in emission, a secure AGN tracer (§5.1).
2. Stacking *Chandra* data of galaxies that were not individually detected in GOODS-N reveals a hard signal and a flat X-ray spectral slope for galaxies that have $P(\text{AGN}) > 30\%$. This suggests that at least some of the 32 galaxies that were stacked do host an actively accreting black hole (§5.2).
3. By combining $[\text{O III}] \lambda 5007$ and hard X-ray luminosities, we calculate a Compton-thickness parameter ($T \equiv L_{2-10\text{keV}}/L_{[\text{O III}] \lambda 5007}$). We identify 33 highly-absorbed AGN candidates. The presence of AGN in at least some of the candidates is supported by the hard X-ray signal ($\Gamma \sim 0.4$) obtained from stacking 13 galaxies that were not detected individually (§6.3). We note that some X-ray galaxies have a steep spectral slope despite a low value of T . These objects are also consistent with the range of values expected from a comparison with known, nearby Compton-thick AGNs (Fig. 11).

- Many absorbed AGNs in the intermediate redshift sample are composite systems, with both star formation and active black hole accretion. The increase in the SF:AGN ratio – and hence a decrease in $[\text{O III}] \lambda 5007/\text{H}\beta$ – may be related to the global rise in the specific star formation rate with redshift. However, the details of such a connection remain open questions (does the host galaxy ISM provide additional AGN absorption? is there a link between host galaxy and torus properties?). The identification of these composites poses a considerable challenge on the observational point-of-view. The MEx probabilistic approach proved to be key in this respect.

On-going and future near-infrared multi-object spectroscopy surveys will shed more light by allowing us to observe all the traditional emission lines directly. The MEx diagram will nevertheless be useful to fill in gaps where $\text{H}\alpha$ and/or $[\text{N II}] \lambda 6584$ fall in especially noisy regions of the spectra or where $[\text{N II}] \lambda 6584$ fails to be detected (as it is typically fainter than $\text{H}\alpha$). In principle, the MEx diagram could be applied out to $z \sim 4$ using near-infrared spectroscopy, thus pushing the limits beyond what will be achievable when relying on $\text{H}\alpha$ and $[\text{N II}] \lambda 6584$ detections (since the latter redshift out of the K -band at $z \sim 2.5$).

We gratefully acknowledge the anonymous referee for useful suggestions that improved this manuscript. The

authors also thank C. Tremonti for kindly providing spectra stellar population fitting routines, M. Cooper for valuable help with the DEEP2 spectra, and E. Daddi for sharing an extended version of his GOODS-North photometric catalog. SJ was partially funded by a FQRNT fellowship (Fonds Québécois de recherche sur la nature et la technologie, Québec, Canada) and a Philanthropic Educational Organization Scholar Award. DMA gratefully acknowledges support from a Royal Society University Research Fellowship and a Philip Leverhulme prize.

The authors would like to thank the many members of the GOODS team who obtained, reduced, and cataloged some of the data used in this paper. This work is based in part on observations made with the *Spitzer* Space Telescope, which is operated by the Jet Propulsion Laboratory, California Institute of Technology under a contract with NASA. Support for this work was provided by NASA through an award issued by JPL/Caltech.

Funding for the DEEP2 survey has been provided by NSF grants AST95-09298, AST-0071048, AST-0071198, AST-0507428, and AST-0507483 as well as NASA LTSA grant NNG04GC89G. The analysis pipeline used to reduce the DEIMOS data was developed at UC Berkeley with support from NSF grant AST-0071048.

Some of the data presented herein were obtained at the W. M. Keck Observatory, which is operated as a scientific partnership among the California Institute of Technology, the University of California and the National Aeronautics and Space Administration. The Observatory was made possible by the generous financial support of the W. M. Keck Foundation. The Keck Observatory acknowledges the very significant cultural role and reverence that the summit of Mauna Kea has always had within the indigenous Hawaiian community and appreciate the opportunity to conduct observations from this mountain.

APPENDIX

COMPARING THE MEX AND CEX DIAGRAMS

The mass-excitation (MEx) and color-excitation (CEx) diagrams are two useful alternatives when the emission lines typically used for AGN diagnostics such as the BPT diagram are not available. The former is developed in this paper (§3.1) and involves using stellar mass as a discriminant between predominantly star-forming galaxies and those hosting an AGN. The CEx diagram was developed by Yan et al. (submitted) and involves using rest-frame $U - B$ color rather than stellar mass. Galaxies hosting an AGN tend to be both massive and redder in $U - B$ so it is not surprising that both these approaches give similar results for many galaxies.

We compared the fraction of galaxies hosting AGN to the purely star-forming galaxies according to the BPT diagram in §3.3. We defined an additional line on the CEx diagram to provide a means to identify a region where star-forming galaxies are mixed with composite galaxies, analogous to our method with the MEx diagram. Here we look at the bivariate distributions of galaxies split into the four categories defined in §3.3. Figure 13 shows that both diagrams are generally comparable. The main dividing lines (upper lines) make a division between the LINERs and Seyfert 2's on the upper side and the star-forming galaxies on the lower side. By design, the MEx diagram selects a larger fraction of the composites in the AGN side. This decision was motivated by our goal to provide an increased completeness of AGN candidates including intrinsically weak as well as absorbed systems that may be undergoing star formation simultaneously with an AGN phase. We have shown the strong potential to find X-ray absorbed candidates among such a population of galaxies (§§5.2,6).

On the CEx diagram, we note a few galaxies in the star-forming category that seem to be outliers with very red $U - B$ colors (also see Figure 5). These may be especially dusty. Their number is small relative to the bulk of the star-forming population in the SDSS sample but they may be interesting targets in a different context. For instance, we may expect more star formation and active galactic nuclei to take place in dusty, infrared-luminous galaxies at higher redshift (Le Floc'h et al. 2005; Magnelli et al. 2009).

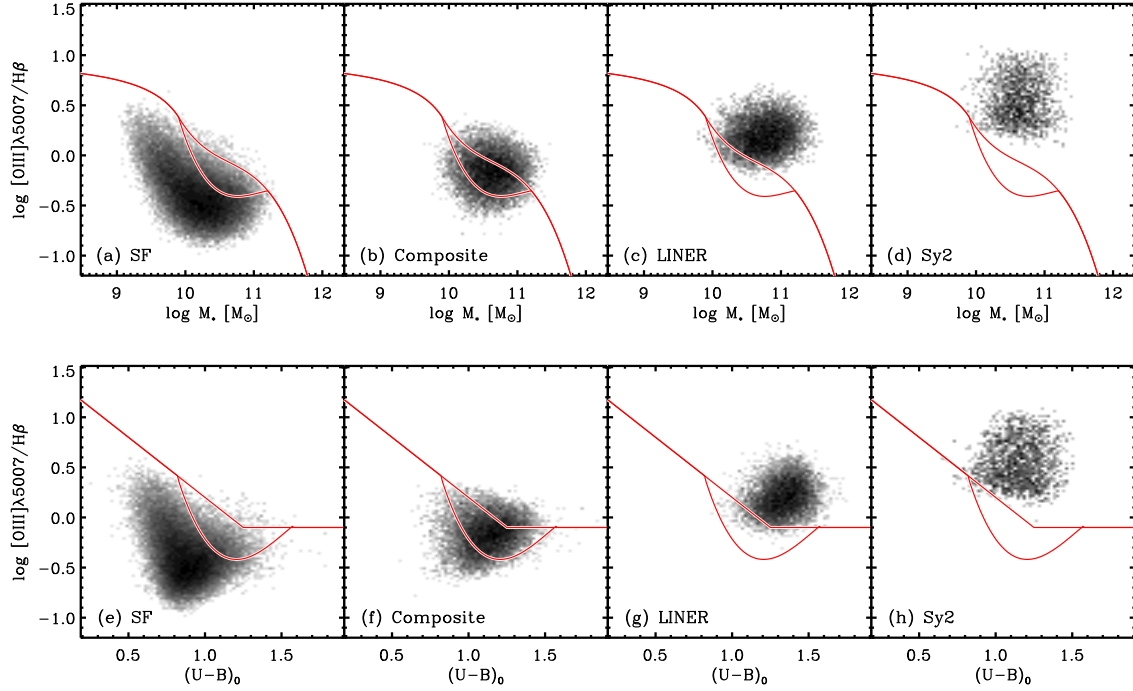


FIG. 13.— Bivariate distributions of the SDSS galaxies on the MEx diagram (top row) and CEx diagram developed by Y11 (bottom row). Galaxies are plotted separately for each classification: (a) star-forming, (b) composite, (c) LINER, and (d) Seyfert 2. The same order is followed in panels (e)-(h) for the CEx diagram. The lower dividing lines were added to mark the region with significant overlap between BPT star-forming and BPT-composite galaxies (the fraction of composites is greater than 40–50% between the lines). (A color version of this figure is available in the online journal.)

STELLAR MASS ESTIMATION

There are 3174 galaxies with both a stellar mass estimate from SED fitting and absolute rest-frame K -band magnitude from observed IRAC photometry. Here, we use EGS galaxies with a SED fit to the FUV, NUV, $ugriz$, and K photometry and GOODS-N galaxies with a SED fit to $UBVRIZJK$ bands (§4.2).

The relation between stellar masses derived from SED fitting and rest-frame K -band absolute magnitudes is displayed in Figure 14. The broken power-law relation is expressed as:

$$\log M_{\star} = -0.398 \times M_K + 1.357; \quad \text{for } M_K > -20.5 \text{ AB} \quad (\text{B1})$$

$$= -0.519 \times M_K - 1.128; \quad \text{for } M_K < -20.5 \text{ AB} \quad (\text{B2})$$

Writing the relation as $M_{\star} \propto L_K^{\alpha}$, the slopes found in Eq. B1 & B2 imply power-law indices $\alpha = 0.99$ at $M_K > -20.5 \text{ AB}$ and $\alpha = 1.3$ at $M_K < -20.5 \text{ AB}$. This relation is linear at the faint end but slightly steeper at the bright end. The steepening of the slope is presumably due to the fact that more massive galaxies are redder owing to the older average age of their stellar populations, and thus have higher mass-to-light ratios.

The residuals of the broken power-law fit (bottom of Figure 14) have a constant scatter with luminosity. The dispersion of the overall sample is 0.18 dex, around the mean (median) of 0.004 (0.009) dex.

Errors on the stellar masses calculated using Eq. B1 & B2 are estimated by combining the average error on $\log(M_{\star})$ from galaxies with SED fitting (0.12 dex) and the dispersion on the $\log(M_{\star}) - M_K$ residuals (0.18 dex). Adding these two contributions in quadrature yields 0.22 dex, which we use for all galaxies lacking a SED fit.

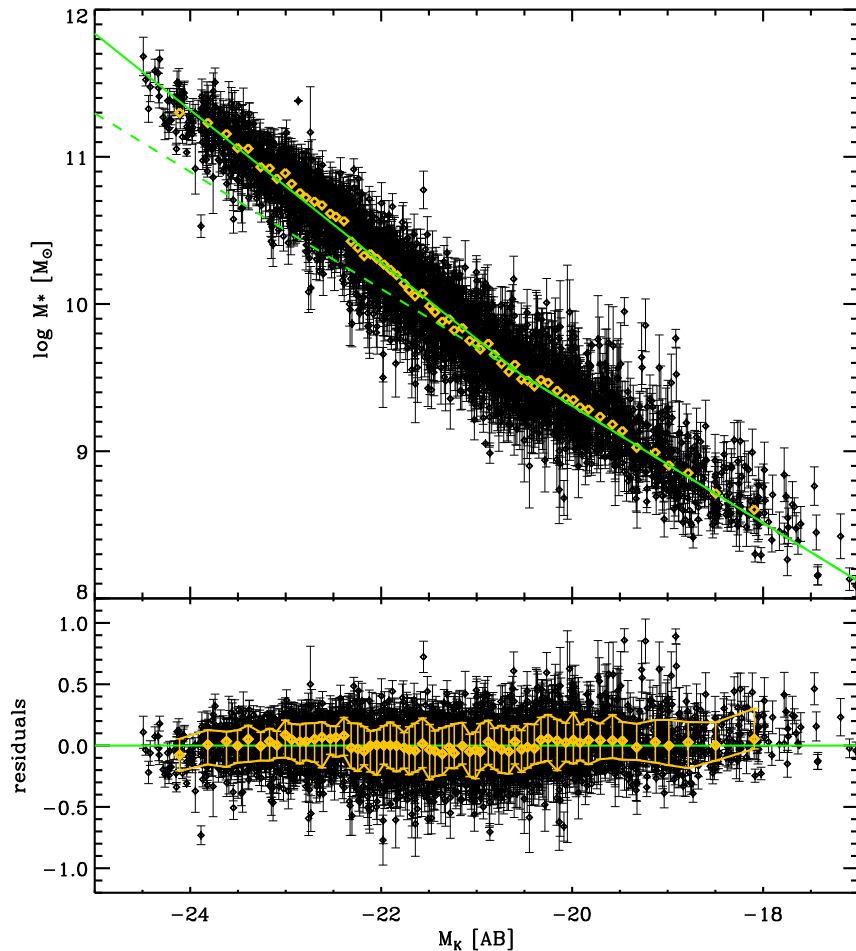


FIG. 14.— [Top] Stellar mass obtained from SED fitting as a function of absolute rest-frame K -band magnitude (M_K , in AB magnitudes). We fit two mass-luminosity power laws for the bright and faint ends, which intersect at $M_K = -20.5 \text{ AB}$ (green lines). The dashed line is the extension of the fit at the faint end, with a linear slope between mass and luminosity. For reference, the yellow diamonds show the median $\log(M_{\star})$ in M_K bins (every 51 points). [Bottom] Residuals of the top panel as a function of M_K . Yellow diamonds and error bars show the median and the 16th to 84th percentile range. There is no obvious trend in the residuals (median=0.009 dex), and the overall dispersion ($\approx (84PL - 16PL)/2$) is 0.18 dex. (A color version of this figure is available in the online journal.)

COMPARISON WITH THE *BLUE* DIAGRAM

The blue diagram discussed in §7.1 was developed in Lamareille et al. (2004) and recently improved in Lamareille (2010). The diagnostic employs lines at blue rest-frame wavelengths, from $[\text{O II}] \lambda 3727$ to $[\text{O III}] \lambda 5007$, in order to facilitate its use out to $z \sim 1$. This motivation is similar to that which guides the design of our MEx diagram, although our results differ significantly.

In this diagnostic, the abscissa is an equivalent width ratio because the spectral separation between the $[\text{O II}] \lambda 3727$ and $\text{H}\beta$ lines is significant and their line flux ratio would thus be very sensitive to dust attenuation. Note the inability to distinguish between SF and Seyfert 2 galaxies in the region marked as SF/Sy2. We show that this ambiguity is completely removed with our new diagram.

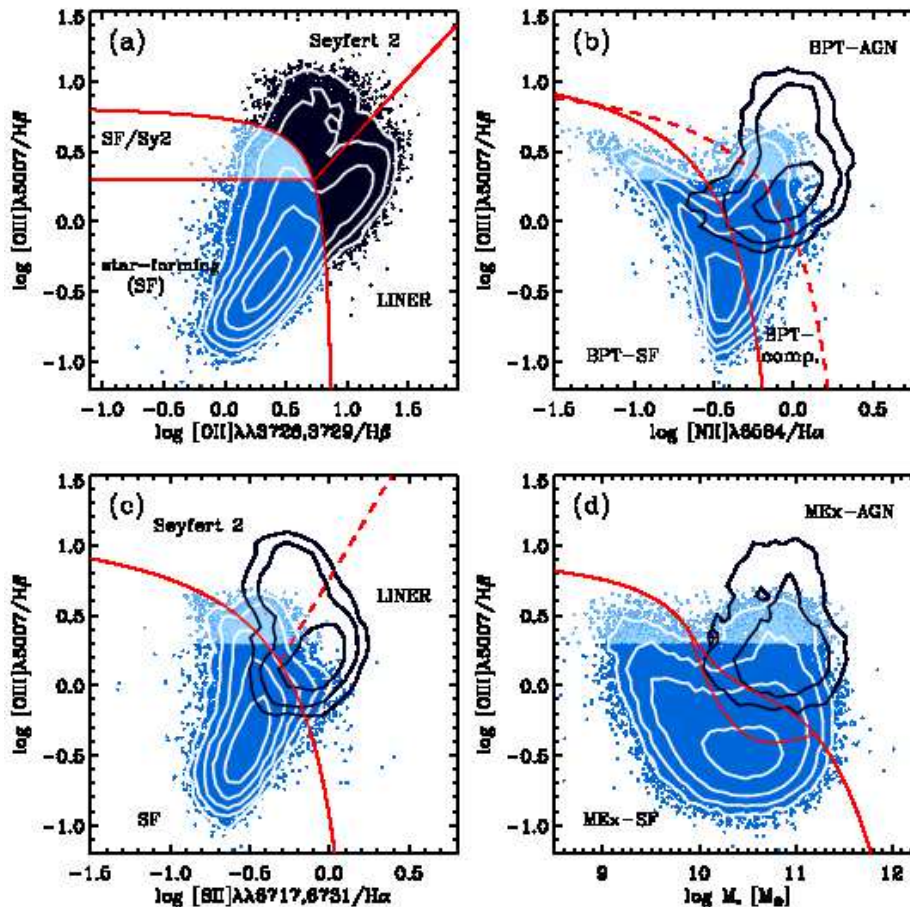


FIG. 15.— Distribution of SDSS galaxies on the blue diagram: $[\text{O III}] \lambda 5007/\text{H}\beta$ line flux ratio against $[\text{O II}] \lambda 3727/\text{H}\beta$ equivalent width ratio. This diagram and dividing lines are adapted from Lamareille (2010). Most star-forming galaxies (SF) occupy the bottom left of the plot (blue dots) but include a number of composite galaxies. The black dots correspond to AGNs (Seyfert 2s and LINERs), and the light blue points mark the galaxies in the region where SF and Sy2 classes overlap. These classifications are compared to other diagnostics: (b) $[\text{N II}]$ BPT diagram, (c) $[\text{S II}]$ BPT diagram, and (d) MEx diagram. The blue diagram star-forming galaxies include a number of composite galaxies as shown on the BPT diagram (b), as well as AGNs that are mostly LINERs according to panel (c). The ambiguous SF/Sy2 galaxies (light blue) are well separated on the other panels, especially (b) and (d). In all panels, the contours indicate the density of points (in bins of $0.075 \text{ dex} \times 0.075 \text{ dex}$) and are logarithmic (0.5 dex apart, with the outermost contour set to 10 galaxies per bin). (A color version of this figure is available in the online journal.)

We examine the selection functions built in the blue diagram against the three other diagnostics introduced earlier. On Figure 15, the blue points represent the star-forming galaxies (panel (a)); note that there is a known overlap with the composite galaxy population as discussed in Lamareille (2010). The pale blue points mark the ambiguous region where SF and Sy2 galaxies are indistinguishable (SF/Sy2) whereas the black dots indicate the AGNs (encompassing both Seyfert 2s and LINERs). Panels (b)-(d) show the location of the same galaxies over the other diagnostic diagrams. The main features are that (i) the ambiguous SF/Sy2 region (pale blue points) is resolved in the other diagrams, which all break the degeneracy observed in the $[\text{O II}] \lambda 3727/\text{H}\beta$ EW ratio of low- M_* SF galaxies and Seyfert 2s; (ii) the blue diagram AGNs (black dots and black contours) include some BPT-composites: more so than the $[\text{S II}]$ -diagram shown in (c), but less so than the BPT (b) and MEx (d) diagrams; and (iii) a large fraction of SF galaxies on the blue diagram are in fact composites or AGNs according to the BPT diagram (b).

The MEx diagram (Figure 6) is applicable to 2,812 galaxies out to $z \sim 1$, whereas the emission lines in the blue

diagram (Figure 16) are only available for 826 galaxies (29%). While 423 out of 531 (80%) GOODS-N galaxies with $H\beta$ and $[O\ III]\ \lambda 5007$ also have a valid measurement of the $[O\ II]\ \lambda 3727$ line, the situation is very different for EGS galaxies. The DEEP2 spectra used for these galaxies span a more restricted range in wavelength and so only 403 among 2,536 objects (16%) with valid $[O\ III]\ \lambda 5007$ and $H\beta$ also have a valid $[O\ II]\ \lambda 3727$ line flux.

The star-forming region of the blue diagram (Figure 16) accounts for 10/13 (77%) of the X-ray starbursts but also for 6/11 (55%) of the X-ray AGNs. The Seyfert 2 region only accounts for 3/11 (27%) of the X-ray AGNs. The smaller number of galaxies on the blue diagram hinder a quantitative comparison with the MEx diagram. Nevertheless, it appears that the former is less reliable at selecting X-ray AGNs.

REFERENCES

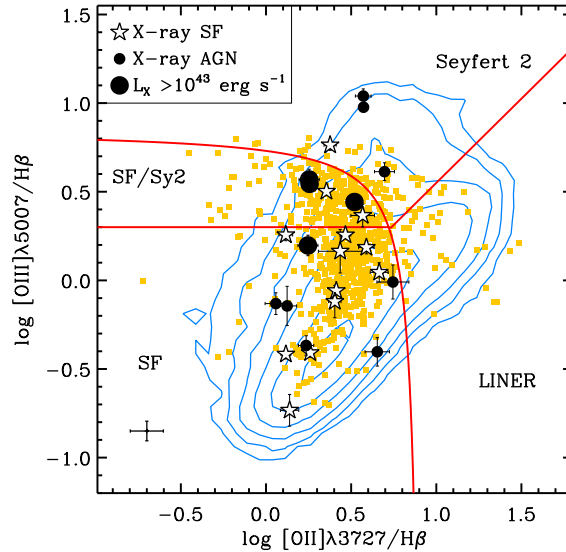


FIG. 16.— The blue diagram, where AGNs are found above the solid curve and further separated between Seyfert 2 and LINER classes, as labeled. Star-forming (SF) galaxies lie below the curve including a region where they are indistinguishable from Seyfert 2 galaxies (labeled as SF/Sy2). In principle, this diagram is applicable out to $z \sim 1$. However, the DEEP2 spectra used in this work span a narrow wavelength range and very few cover all three lines required in this diagram. While performing well at selecting the X-ray starbursts (star symbols), this diagram misses the majority of X-ray AGNs (filled black circles) including the brighter ones (larger circles). Contours show the SDSS low- z sample (evenly spaced on a logarithmic scale). Our intermediate redshift sample is superimposed (orange points) and, when available, the X-ray classification is marked with larger symbols [star symbols for X-ray starbursts; small (large) filled circles for X-ray AGNs with $L_X < 10^{43}$ erg s^{-1} ($L_X > 10^{43}$ erg s^{-1})]. (A color version of this figure is available in the online journal.)

- Adelman-McCarthy, J. K., Agüeros, M. A., Allam, S. S., Anderson, K. S. J., Anderson, S. F., Annis, J., Bahcall, N. A., Baldry, I. K., Barentine, J. C., Berlind, A., Bernardi, M., Blanton, M. R., Boroski, W. N., Brewington, H. J., Brinchmann, J., Brinkmann, J., Brunner, R. J., Budavári, T., Carey, L. N., Carr, M. A., Castander, F. J., Connolly, A. J., Csabai, I., Czarapata, P. C., Dalcanton, J. J., Doi, M., Dong, F., Eisenstein, D. J., Evans, M. L., Fan, X., Finkbeiner, D. P., Friedman, S. D., Frieman, J. A., Fukugita, M., Gillespie, B., Glazebrook, K., Gray, J., Grebel, E. K., Gunn, J. E., Gurbani, V. K., de Haas, E., Hall, P. B., Harris, F. H., Harvanek, M., Hawley, S. L., Hayes, J., Hendry, J. S., Hennessy, G. S., Hindsley, R. B., Hirata, C. M., Hogan, C. J., Hogg, D. W., Holmgren, D. J., Holtzman, J. A., Ichikawa, S., Ivezić, Ž., Jester, S., Johnston, D. E., Jorgensen, A. M., Jurić, M., Kent, S. M., Kleinman, S. J., Knapp, G. R., Kniazev, A. Y., Kron, R. G., Krzesinski, J., Kuropatkin, N., Lamb, D. Q., Lampeitl, H., Lee, B. C., Leger, R. F., Lin, H., Long, D. C., Loveday, J., Lupton, R. H., Margon, B., Martínez-Delgado, D., Mandelbaum, R., Matsubara, T., McGehee, P. M., McKay, T. A., Meiksin, A., Munn, J. A., Nakajima, R., Nash, T., Neilsen, Jr., E. H., Newberg, H. J., Newman, P. R., Nichol, R. C., Nicinski, T., Nieto-Santisteban, M., Nitta, A., O'Mullane, W., Okamura, S., Owen, R., Padmanabhan, N., Pauls, G., Peoples, Jr., J., Pier, J. R., Pope, A. C., Pourbaix, D., Quinn, T. R., Richards, G. T., Richmond, M. W., Rockosi, C. M., Schlegel, D. J., Schneider, D. P., Schroeder, J., Scranton, R., Seljak, U., Sheldon, E., Shimasaku, K., Smith, J. A., Smolčić, V., Snedden, S. A., Stoughton, C., Strauss, M. A., SubbaRao, M., Szalay, A. S., Szapudi, I., Szkody, P., Tegmark, M., Thakar, A. R., Tucker, D. L., Uomoto, A., Vanden Berk, D. E., Vandenberg, J., Vogeley, M. S., Voges, W., Vogt, N. P., Walkowicz, L. M., Weinberg, D. H., West, A. A., White, S. D. M., Xu, Y., Yanny, B., Yocum, D. R., York, D. G., Zehavi, I., Zibetti, S., & Zucker, D. B. 2006, *ApJS*, 162, 38
- Akyas, A. & Georgantopoulos, I. 2009, *A&A*, 500, 999
- Alexander, D. M., Bauer, F. E., Brandt, W. N., Schneider, D. P., Hornschemeier, A. E., Vignali, C., Barger, A. J., Broos, P. S., Cowie, L. L., Garmire, G. P., Townsley, L. K., Bautz, M. W., Chartas, G., & Sargent, W. L. W. 2003, *AJ*, 126, 539
- Alexander, D. M., Bauer, F. E., Chapman, S. C., Smail, I., Blain, A. W., Brandt, W. N., & Ivison, R. J. 2005, *ApJ*, 632, 736
- Antonucci, R. 1993, *ARA&A*, 31, 473
- Armus, L., Charmandaris, V., Bernard-Salas, J., Spoon, H. W. W., Marshall, J. A., Higdon, S. J. U., Desai, V., Teplitz, H. I., Hao, L., Devost, D., Brandl, B. R., Wu, Y., Sloan, G. C., Soifer, B. T., Houck, J. R., & Herter, T. L. 2007, *ApJ*, 656, 148
- Armus, L., Charmandaris, V., Spoon, H. W. W., Houck, J. R., Soifer, B. T., Brandl, B. R., Appleton, P. N., Teplitz, H. I., Higdon, S. J. U., Weedman, D. W., Devost, D., Morris, P. W., Uchida, K. I., van Cleve, J., Barry, D. J., Sloan, G. C., Grillmair, C. J., Burgdorf, M. J., Fajardo-Acosta, S. B., Ingalls, J. G., Higdon, J., Hao, L., Bernard-Salas, J., Herter, T., Troeltzsch, J., Unruh, B., & Winghart, M. 2004, *ApJS*, 154, 178
- Bade, N., Fink, H. H., Engels, D., Voges, W., Hagen, H., Wisotzki, L., & Reimers, D. 1995, *A&AS*, 110, 469
- Baldwin, J. A., Phillips, M. M., & Terlevich, R. 1981, *PASP*, 93, 5
- Barger, A. J., Cowie, L. L., Bautz, M. W., Brandt, W. N., Garmire, G. P., Hornschemeier, A. E., Ivison, R. J., & Owen, F. N. 2001, *AJ*, 122, 2177
- Barmby, P., Huang, J.-S., Ashby, M. L. N., Eisenhardt, P. R. M., Fazio, G. G., Willner, S. P., & Wright, E. L. 2008, *ApJS*, 177, 431
- Bassani, L., Dadina, M., Maiolino, R., Salvati, M., Risaliti, G., della Ceca, R., Matt, G., & Zamorani, G. 1999, *ApJS*, 121, 473

- Bauer, F. E., Alexander, D. M., Brandt, W. N., Schneider, D. P., Treister, E., Hornschemeier, A. E., & Garmire, G. P. 2004, *AJ*, 128, 2048
- Binette, L., Magris, C. G., Stasińska, G., & Bruzual, A. G. 1994, *A&A*, 292, 13
- Blanton, M. R. & Roweis, S. 2007, *AJ*, 133, 734
- Boyle, B. J., Griffiths, R. E., Shanks, T., Stewart, G. C., & Georgantopoulos, I. 1993, *MNRAS*, 260, 49
- Brandt, W. N., Alexander, D. M., Hornschemeier, A. E., Garmire, G. P., Schneider, D. P., Barger, A. J., Bauer, F. E., Broos, P. S., Cowie, L. L., Townsley, L. K., Burrows, D. N., Chartas, G., Feigelson, E. D., Griffiths, R. E., Nousek, J. A., & Sargent, W. L. W. 2001, *AJ*, 122, 2810
- Brinchmann, J., Pettini, M., & Charlot, S. 2008, *MNRAS*, 385, 769
- Bruzual, G. & Charlot, S. 2003, *MNRAS*, 344, 1000
- Bundy, K., Ellis, R. S., Conselice, C. J., Taylor, J. E., Cooper, M. C., Willmer, C. N. A., Weiner, B. J., Coil, A. L., Noeske, K. G., & Eisenhardt, P. R. M. 2006, *ApJ*, 651, 120
- Busko, I. C. & Steiner, J. E. 1988, *MNRAS*, 232, 525
- Capak, P., Cowie, L. L., Hu, E. M., Barger, A. J., Dickinson, M., Fernandez, E., Giavalisco, M., Komiyama, Y., Kretchmer, C., McNally, C., Miyazaki, S., Okamura, S., & Stern, D. 2004, *AJ*, 127, 180
- Chabrier, G. 2003, *PASP*, 115, 763
- Coil, A. L., Georgakakis, A., Newman, J. A., Cooper, M. C., Croton, D., Davis, M., Koo, D. C., Laird, E. S., Nandra, K., Weiner, B. J., Willmer, C. N. A., & Yan, R. 2009, *ApJ*, 701, 1484
- Coil, A. L., Newman, J. A., Kaiser, N., Davis, M., Ma, C., Kocevski, D. D., & Koo, D. C. 2004, *ApJ*, 617, 765
- Comastri, A., Setti, G., Zamorani, G., & Hasinger, G. 1995, *A&A*, 296, 1
- Croton, D. J., Springel, V., White, S. D. M., De Lucia, G., Frenk, C. S., Gao, L., Jenkins, A., Kauffmann, G., Navarro, J. F., & Yoshida, N. 2006, *MNRAS*, 365, 11
- Daddi, E., Bournaud, F., Walter, F., Dannerbauer, H., Carilli, C. L., Dickinson, M., Elbaz, D., Morrison, G. E., Riechers, D., Onodera, M., Salmi, F., Krips, M., & Stern, D. 2010, *ApJ*, 713, 686
- Daddi, E., Dickinson, M., Morrison, G., Chary, R., Cimatti, A., Elbaz, D., Frayer, D., Renzini, A., Pope, A., Alexander, D. M., Bauer, F. E., Giavalisco, M., Huynh, M., Kurk, J., & Mignoli, M. 2007, *ApJ*, 670, 156
- Davis, M., Faber, S. M., Newman, J., Phillips, A. C., Ellis, R. S., Steidel, C. C., Conselice, C., Coil, A. L., Finkbeiner, D. P., Koo, D. C., Guhathakurta, P., Weiner, B., Schiavon, R., Willmer, C., Kaiser, N., Luppino, G. A., Wirth, G., Connolly, A., Eisenhardt, P., Cooper, M., & Gerke, B. 2003, in Presented at the Society of Photo-Optical Instrumentation Engineers (SPIE) Conference, Vol. 4834, Society of Photo-Optical Instrumentation Engineers (SPIE) Conference Series, ed. P. Guhathakurta, 161–172
- Davis, M., Guhathakurta, P., Konidaris, N. P., Newman, J. A., Ashby, M. L. N., Biggs, A. D., Barmby, P., Bundy, K., Chapman, S. C., Coil, A. L., Conselice, C. J., Cooper, M. C., Croton, D. J., Eisenhardt, P. R. M., Ellis, R. S., Faber, S. M., Fang, T., Fazio, G. G., Georgakakis, A., Gerke, B. F., Goss, W. M., Gwyn, S., Harker, J., Hopkins, A. M., Huang, J.-S., Ivison, R. J., Kassin, S. A., Kirby, E. N., Koekemoer, A. M., Koo, D. C., Laird, E. S., Le Floch, E., Lin, L., Lotz, J. M., Marshall, P. J., Martin, D. C., Metevier, A. J., Moustakas, L. A., Nandra, K., Noeske, K. G., Papovich, C., Phillips, A. C., Rich, R. M., Rieke, G. H., Rigopoulou, D., Salim, S., Schiminovich, D., Simard, L., Smail, I., Small, T. A., Weiner, B. J., Willmer, C. N. A., Willner, S. P., Wilson, G., Wright, E. L., & Yan, R. 2007, *ApJ*, 660, L1
- Di Matteo, T., Springel, V., & Hernquist, L. 2005, *Nature*, 433, 604
- Diamond-Stanic, A. M., Rieke, G. H., & Rigby, J. R. 2009, *ApJ*, 698, 623
- Donley, J. L., Rieke, G. H., Pérez-González, P. G., Rigby, J. R., & Alonso-Herrero, A. 2007, *ApJ*, 660, 167
- Dudik, R. P., Satyapal, S., & Marcu, D. 2009, *ApJ*, 691, 1501
- Elbaz, D., Daddi, E., Le Borgne, D., Dickinson, M., Alexander, D. M., Chary, R., Starck, J., Brandt, W. N., Kitzbichler, M., MacDonald, E., Nonino, M., Popesso, P., Stern, D., & Vanzella, E. 2007, *A&A*, 468, 33
- Eracleous, M., Hwang, J. A., & Flohic, H. M. L. G. 2010, *ApJ*, 711, 796
- Faber, S. M., Phillips, A. C., Kibrick, R. I., Alcott, B., Allen, S. L., Burrous, J., Cantrall, T., Clarke, D., Coil, A. L., Cowley, D. J., Davis, M., Deich, W. T. S., Dietsch, K., Gilmore, D. K., Harper, C. A., Hilyard, D. F., Lewis, J. P., McVeigh, M., Newman, J., Osborne, J., Schiavon, R., Stover, R. J., Tucker, D., Wallace, V., Wei, M., Wirth, G., & Wright, C. A. 2003, in Presented at the Society of Photo-Optical Instrumentation Engineers (SPIE) Conference, Vol. 4841, Society of Photo-Optical Instrumentation Engineers (SPIE) Conference Series, ed. M. Iye & A. F. M. Moorwood, 1657–1669
- Fabian, A. C. 1999, *MNRAS*, 308, L39
- Ferrarese, L. & Merritt, D. 2000, *ApJ*, 539, L9
- Genzel, R., Lutz, D., Sturm, E., Egami, E., Kunze, D., Moorwood, A. F. M., Rigopoulou, D., Spoon, H. W. W., Sternberg, A., Tacconi-Garman, L. E., Tacconi, L., & Thatte, N. 1998, *ApJ*, 498, 579
- Goulding, A. D. & Alexander, D. M. 2009, *MNRAS*, 398, 1165
- Groves, B. A., Heckman, T. M., & Kauffmann, G. 2006, *MNRAS*, 371, 1559
- Guainazzi, M., Molendi, S., Vignati, P., Matt, G., & Iwasawa, K. 2000, *New Astronomy*, 5, 235
- Gwyn, S. D. J. 2008, *PASP*, 120, 212
- . 2011, *ArXiv e-prints*
- Hainline, K. N., Shapley, A. E., Kornei, K. A., Pettini, M., Buckley-Geer, E., Allam, S. S., & Tucker, D. L. 2009, *ApJ*, 701, 52
- Heckman, T. M. 1980, *A&A*, 87, 152
- Heckman, T. M., Ptak, A., Hornschemeier, A., & Kauffmann, G. 2005, *ApJ*, 634, 161
- Ho, L. C. 1999, *Advances in Space Research*, 23, 813
- . 2008, *ARA&A*, 46, 475
- Ho, L. C., Filippenko, A. V., & Sargent, W. L. W. 1993, *ApJ*, 417, 63
- Hopkins, P. F., Hernquist, L., Cox, T. J., Di Matteo, T., Martini, P., Robertson, B., & Springel, V. 2005, *ApJ*, 630, 705
- Hopkins, P. F. & Quataert, E. 2010, *MNRAS*, 407, 1529
- Kauffmann, G., Heckman, T. M., White, S. D. M., Charlot, S., Tremonti, C., Brinchmann, J., Bruzual, G., Peng, E. W., Seibert, M., Bernardi, M., Blanton, M., Brinkmann, J., Castander, F., Csábai, I., Fukugita, M., Ivezić, Z., Munn, J. A., Nichol, R. C., Padmanabhan, N., Thakar, A. R., Weinberg, D. H., & York, D. 2003, *MNRAS*, 341, 33
- Kauffmann et al., G. 2003, *MNRAS*, 346, 1055
- Kewley, L. J., Dopita, M. A., Sutherland, R. S., Heisler, C. A., & Trevena, J. 2001, *ApJ*, 556, 121
- Kewley, L. J. & Ellison, S. L. 2008, *ApJ*, 681, 1183
- Kewley, L. J., Groves, B., Kauffmann, G., & Heckman, T. 2006, *MNRAS*, 372, 961
- Kroupa, P. 2001, *MNRAS*, 322, 231
- Lacy, M., Storrie-Lombardi, L. J., Sajina, A., Appleton, P. N., Armus, L., Chapman, S. C., Choi, P. I., Fadda, D., Fang, F., Frayer, D. T., Heinrichsen, I., Helou, G., Im, M., Marleau, F. R., Masci, F., Shupe, D. L., Soifer, B. T., Surace, J., Teplitz, H. I., Wilson, G., & Yan, L. 2004, *ApJS*, 154, 166
- Laird, E. S., Nandra, K., Georgakakis, A., Aird, J. A., Barmby, P., Conselice, C. J., Coil, A. L., Davis, M., Faber, S. M., Fazio, G. G., Guhathakurta, P., Koo, D. C., Sarajedini, V., & Willmer, C. N. A. 2009, *ApJS*, 180, 102
- Lamareille, F. 2010, *A&A*, 509, A53+
- Lamareille, F., Mouhcine, M., Contini, T., Lewis, I., & Maddox, S. 2004, *MNRAS*, 350, 396
- LaMassa, S. M., Heckman, T. M., Ptak, A., Hornschemeier, A., Martins, L., Sonnentrucker, P., & Tremonti, C. 2009, *ApJ*, 705, 568
- LaMassa, S. M., Heckman, T. M., Ptak, A., Martins, L., Wild, V., & Sonnentrucker, P. 2010, *ApJ*, 720, 786
- Le Floch, E., Papovich, C., Dole, H., Bell, E. F., Lagache, G., Rieke, G. H., Egami, E., Pérez-González, P. G., Alonso-Herrero, A., Rieke, M. J., Blaylock, M., Engelbracht, C. W., Gordon, K. D., Hines, D. C., Misselt, K. A., Morrison, J. E., & Mould, J. 2005, *ApJ*, 632, 169

- Liu, X., Shapley, A. E., Coil, A. L., Brinchmann, J., & Ma, C. 2008, *ApJ*, 678, 758
- Lutz, D., Spoon, H. W. W., Rigopoulou, D., Moorwood, A. F. M., & Genzel, R. 1998, *ApJ*, 505, L103
- Magnelli, B., Elbaz, D., Chary, R. R., Dickinson, M., Le Borgne, D., Frayer, D. T., & Willmer, C. N. A. 2009, *A&A*, 496, 57
- Magorrian, J., Tremaine, S., Richstone, D., Bender, R., Bower, G., Dressler, A., Faber, S. M., Gebhardt, K., Green, R., Grillmair, C., Kormendy, J., & Lauer, T. 1998, *AJ*, 115, 2285
- Maiolino, R. & Rieke, G. H. 1995, *ApJ*, 454, 95
- Maiolino, R., Salvati, M., Bassani, L., Dadina, M., della Ceca, R., Matt, G., Risaliti, G., & Zamorani, G. 1998, *A&A*, 338, 781
- Malkan, M. A., Gorjian, V., & Tam, R. 1998, *ApJS*, 117, 25
- Matt, G., Fabian, A. C., Guainazzi, M., Iwasawa, K., Bassani, L., & Malaguti, G. 2000, *MNRAS*, 318, 173
- Mulchaey, J. S., Koratkar, A., Ward, M. J., Wilson, A. S., Whittle, M., Antonucci, R. R. J., Kinney, A. L., & Hurt, T. 1994, *ApJ*, 436, 586
- Mullaney, J. R., Alexander, D. M., Huynh, M., Goulding, A. D., & Frayer, D. 2010, *MNRAS*, 401, 995
- Mushotzky, R. F., Cowie, L. L., Barger, A. J., & Arnaud, K. A. 2000, *Nature*, 404, 459
- Nandra, K., Laird, E. S., Adelberger, K., Gardner, J. P., Mushotzky, R. F., Rhodes, J., Steidel, C. C., Teplitz, H. I., & Arnaud, K. A. 2005, *MNRAS*, 356, 568
- Narayanan, D., Cox, T. J., Kelly, B., Davé, R., Hernquist, L., Di Matteo, T., Hopkins, P. F., Kulesa, C., Robertson, B., & Walker, C. K. 2008, *ApJS*, 176, 331
- Noeske, K. G., Weiner, B. J., Faber, S. M., Papovich, C., Koo, D. C., Somerville, R. S., Bundy, K., Conselice, C. J., Newman, J. A., Schiminovich, D., Le Floch, E., Coil, A. L., Rieke, G. H., Lotz, J. M., Primack, J. R., Barmby, P., Cooper, M. C., Davis, M., Ellis, R. S., Fazio, G. G., Guhathakurta, P., Huang, J., Kassin, S. A., Martin, D. C., Phillips, A. C., Rich, R. M., Small, T. A., Willmer, C. N. A., & Wilson, G. 2007, *ApJ*, 660, L43
- Pope, A., Chary, R., Alexander, D. M., Armus, L., Dickinson, M., Elbaz, D., Frayer, D., Scott, D., & Teplitz, H. 2008, *ApJ*, 675, 1171
- Richstone, D., Ajhar, E. A., Bender, R., Bower, G., Dressler, A., Faber, S. M., Filippenko, A. V., Gebhardt, K., Green, R., Ho, L. C., Kormendy, J., Lauer, T. R., Magorrian, J., & Tremaine, S. 1998, *Nature*, 395, A14+
- Rigby, J. R., Diamond-Stanic, A. M., & Aniano, G. 2009, *ApJ*, 700, 1878
- Rigby, J. R., Rieke, G. H., Donley, J. L., Alonso-Herrero, A., & Pérez-González, P. G. 2006, *ApJ*, 645, 115
- Salim, S., Charlot, S., Rich, R. M., Kauffmann, G., Heckman, T. M., Barlow, T. A., Bianchi, L., Byun, Y., Donas, J., Forster, K., Friedman, P. G., Jelinsky, P. N., Lee, Y., Madore, B. F., Malina, R. F., Martin, D. C., Milliard, B., Morrissey, P., Neff, S. G., Schiminovich, D., Seibert, M., Siegmund, O. H. W., Small, T., Szalay, A. S., Welsh, B. Y., & Wyder, T. K. 2005, *ApJ*, 619, L39
- Salim, S., Dickinson, M., Michael Rich, R., Charlot, S., Lee, J. C., Schiminovich, D., Pérez-González, P. G., Ashby, M. L. N., Papovich, C., Faber, S. M., Ivison, R. J., Frayer, D. T., Walton, J. M., Weiner, B. J., Chary, R., Bundy, K., Noeske, K., & Koekemoer, A. M. 2009, *ApJ*, 700, 161
- Salim, S., Rich, R. M., Charlot, S., Brinchmann, J., Johnson, B. D., Schiminovich, D., Seibert, M., Mallery, R., Heckman, T. M., Forster, K., Friedman, P. G., Martin, D. C., Morrissey, P., Neff, S. G., Small, T., Wyder, T. K., Bianchi, L., Donas, J., Lee, Y., Madore, B. F., Milliard, B., Szalay, A. S., Welsh, B. Y., & Yi, S. K. 2007, *ApJS*, 173, 267
- Sanders, D. B. & Mirabel, I. F. 1996, *ARA&A*, 34, 749
- Sanders, D. B., Soifer, B. T., Elias, J. H., Madore, B. F., Matthews, K., Neugebauer, G., & Scoville, N. Z. 1988, *ApJ*, 325, 74
- Savaglio, S., Glazebrook, K., Le Borgne, D., Juneau, S., Abraham, R. G., Chen, H., Crampton, D., McCarthy, P. J., Carlberg, R. G., Marzke, R. O., Roth, K., Jørgensen, I., & Murowinski, R. 2005, *ApJ*, 635, 260
- Seyfert, C. K. 1943, *ApJ*, 97, 28
- Stasińska, G., Cid Fernandes, R., Mateus, A., Sodr e, L., & Asari, N. V. 2006, *MNRAS*, 371, 972
- Stasińska, G., Vale Asari, N., Cid Fernandes, R., Gomes, J. M., Schlickmann, M., Mateus, A., Schoenell, W., & Sodr e, Jr., L. 2008, *MNRAS*, 391, L29
- Stern, D., Eisenhardt, P., Gorjian, V., Kochanek, C. S., Caldwell, N., Eisenstein, D., Brodwin, M., Brown, M. J. I., Cool, R., Dey, A., Green, P., Jannuzi, B. T., Murray, S. S., Pahre, M. A., & Willner, S. P. 2005, *ApJ*, 631, 163
- Sturm, E., Lutz, D., Verma, A., Netzer, H., Sternberg, A., Moorwood, A. F. M., Oliva, E., & Genzel, R. 2002, *A&A*, 393, 821
- Tacconi, L. J., Genzel, R., Neri, R., Cox, P., Cooper, M. C., Shapiro, K., Bolatto, A., Bouch e, N., Bournaud, F., Burkert, A., Combes, F., Comerford, J., Davis, M., Schreiber, N. M. F., Garcia-Burillo, S., Gracia-Carpio, J., Lutz, D., Naab, T., Omont, A., Shapley, A., Sternberg, A., & Weiner, B. 2010, *Nature*, 463, 781
- Teister, E. & Urry, C. M. 2005, *ApJ*, 630, 115
- Tremonti, C. A., Heckman, T. M., Kauffmann, G., Brinchmann, J., Charlot, S., White, S. D. M., Seibert, M., Peng, E. W., Schlegel, D. J., Uomoto, A., Fukugita, M., & Brinkmann, J. 2004, *ApJ*, 613, 898
- Tremonti, C. A., Moustakas, J., & Diamond-Stanic, A. M. 2007, *ApJ*, 663, L77
- Trump, J. R., Impey, C. D., Taniguchi, Y., Brusa, M., Civano, F., Elvis, M., Gabor, J. M., Jahnke, K., Kelly, B. C., Koekemoer, A. M., Nagao, T., Salvato, M., Shioya, Y., Capak, P., Huchra, J. P., Kartaltepe, J. S., Lanzuisi, G., McCarthy, P. J., Mainieri, V., & Scoville, N. Z. 2009, *ApJ*, 706, 797
- Veilleux, S. & Osterbrock, D. E. 1987, *ApJS*, 63, 295
- Vignali, C., Alexander, D. M., Gilli, R., & Pozzi, F. 2010, *MNRAS*, 404, 48
- Weiner, B. J., Papovich, C., Bundy, K., Conselice, C. J., Cooper, M. C., Ellis, R. S., Ivison, R. J., Noeske, K. G., Phillips, A. C., & Yan, R. 2007, *ApJ*, 660, L39
- Wirth, G. D., Willmer, C. N. A., Amico, P., Chaffee, F. H., Goodrich, R. W., Kwok, S., Lyke, J. E., Mader, J. A., Tran, H. D., Barger, A. J., Cowie, L. L., Capak, P., Coil, A. L., Cooper, M. C., Conrad, A., Davis, M., Faber, S. M., Hu, E. M., Koo, D. C., Le Mignant, D., Newman, J. A., & Songaila, A. 2004, *AJ*, 127, 3121
- Worsley, M. A., Fabian, A. C., Bauer, F. E., Alexander, D. M., Hasinger, G., Mateos, S., Brunner, H., Brandt, W. N., & Schneider, D. P. 2005, *MNRAS*, 357, 1281
- Wright, S. A., Larkin, J. E., Graham, J. R., & Ma, C. 2010, *ApJ*, 711, 1291
- Yan, R., Ho, L. C., Newman, J. A., Coil, A. L., Willmer, C. N. A., Laird, E. S., Georgakakis, A., Aird, J., Barmby, P., Bundy, K., Cooper, M. C., Davis, M., Faber, S. M., Fang, T., Griffith, R. L., Koekemoer, A. M., Koo, D. C., Nandra, K., Park, S. Q., Sarajedini, V. L., Weiner, B. J., & Willner, S. P. 2011, *ApJ*, 728, 38
- York, D. G., Adelman, J., Anderson, Jr., J. E., Anderson, S. F., Annis, J., Bahcall, N. A., Bakken, J. A., Barkhouser, R., & others. 2000, *AJ*, 120, 1579
- Yuan, T., Kewley, L. J., & Sanders, D. B. 2010, *ApJ*, 709, 884

TABLE 1
DEMOGRAPHICS OF THE MEX DIAGRAM

| BPT type | MEx-AGN | (%) | MEx-Interm. ^a | (%) | MEx-SF | (%) |
|---------------|---------|------|--------------------------|------|--------|------|
| BPT-SF | 1465 | 6.0 | 9153 | 51.7 | 64243 | 94.4 |
| BPT-composite | 9782 | 40.0 | 8468 | 47.8 | 3760 | 5.5 |
| BPT-AGN | 13212 | 54.0 | 90 | 0.5 | 31 | 0.04 |
| All | 24459 | 100 | 17711 | 100 | 68034 | 100 |

^a MEx-intermediate region: between the two curves defined by Equations 1 and 2.

TABLE 2
X-RAY STACKING OF NON-DETECTIONS

| Sample | N ^a | $\langle z \rangle$ | Soft ^b | Soft σ | Hard ^b | Hard σ | HR ^c | Γ^d | Comment |
|---|----------------|---------------------|-------------------|------------------|-------------------|------------------|-----------------|------------|---|
| (i) MEx Diagram Selection (see §5.2) | | | | | | | | | |
| P(AGN) \geq 50% | 22 | 0.70 ± 0.18 | 1.61 ± 0.54 | 4.6 | 1.61 ± 0.81 | 2.9 | 0.00 | 0.8 | Many absorbed AGNs |
| P(SF) $>$ 50% | 25 | 0.60 ± 0.19 | 2.20 ± 0.54 | 6.3 | 1.49 ± 0.81 | 2.7 | -0.19 | 1.2 | Star-forming galaxies and some absorbed AGNs |
| P(AGN) \geq 30% | 34 | 0.72 ± 0.17 | 1.31 ± 0.45 | 4.4 | 1.67 ± 0.69 | 3.6 | 0.12 | 0.8 | Many absorbed AGNs |
| P(SF) $>$ 70% | 13 | 0.54 ± 0.15 | 2.78 ± 0.77 | 5.8 | 1.03 ± 1.10 | 1.4 | -0.46 | 1.7 | Mostly star-forming galaxies |
| $30\% \leq$ P(AGN) $<$ 50% | 12 | 0.77 ± 0.14 | 1.56 ± 0.77 | 3.1 | 2.1 ± 1.2 | 2.6 | 0.15 | 0.6 | Many absorbed AGNs |
| (ii) Absorbed AGN Selection (based on $T \equiv L_{2-10\text{keV}}/L_{[\text{O III}]\lambda 5007}$, see §6.3) | | | | | | | | | |
| $\log(T) < 0.25^e$ | 13 | 0.71 ± 0.19 | 1.72 ± 0.68 | 3.9 | 2.7 ± 1.0 | 4.0 | 0.22 | 0.4 | Very absorbed AGNs |

^a Number of galaxies in the X-ray stack.

^b Count rate in units of 10^{-6} count s^{-1} .

^c Hardness Ratio \equiv (H-S)/(H+S), where H and S are the X-ray counts in the hard (2-8 keV) and soft (0.5-2 keV) bands.

^d Effective Photon Index.

^e Also required P(AGN) $>$ 30% and $\log(M_* [M_\odot]) > 10.2$ as selection criteria.